Structural basis for PRC2 decoding of active histone methylation marks H3K36me2/3

Ksenia Finogenova(1), Jacques Bonnet (1), Simon Poepsel(2,3), Ingmar B. Schäfer(4), Katja Finkl(1), Katharina Schmid(1), Claudia Litz(1), Mike Strauss(5,6), Christian Benda(4) and Jürg Müller(1)

1) Max Planck Institute of Biochemistry, Laboratory of Chromatin Biology, Martinsried, Germany
2) California Institute for Quantitative Biology (QB3), University of California, Berkeley, Molecular Biophysics and Integrative Bio-Imaging Division, Lawrence Berkeley National Laboratory, Berkeley, CA
3) University of Cologne, Center for Molecular Medicine Cologne (CMMC), Faculty of Medicine and University Hospital Cologne, Cologne, Germany, Cologne Excellence Cluster for Cellular Stress Responses in Ageing-Associated Diseases (CECAD), University of Cologne, Cologne, Germany
4) Max Planck Institute of Biochemistry, Department of Structural Cell Biology, Martinsried, Germany
5) Max Planck Institute of Biochemistry, cryoEM Facility, Martinsried, Germany
6) Current address: McGill University, Department of Anatomy and Cell Biology, Montreal, Canada

Correspondence should be addressed to J.M. (muellerj@biochem.mpg.de)

ABSTRACT

Repression of genes by Polycomb requires that PRC2 modifies their chromatin by trimethylating lysine 27 on histone H3 (H3K27me3). At transcriptionally active genes, di- and trimethylated H3K36 inhibit PRC2. Here, the cryo-EM structure of PRC2 on dinucleosomes reveals how binding of its catalytic subunit EZH2 to nucleosomal DNA orients the H3 N-terminus via an extended network of interactions to place H3K27 into the active site. Unmodified H3K36 occupies a critical position in the EZH2-DNA interface. Mutation of H3K36 to arginine or alanine inhibits H3K27 methylation by PRC2 on nucleosomes *in vitro*. Accordingly, *Drosophila* H3K36A and H3K36R mutants show reduced levels of H3K27me3 and defective Polycomb repression of HOX genes. The relay of interactions between EZH2, the nucleosomal DNA and the H3 N-terminus therefore creates the geometry that permits allosteric inhibition of PRC2 by methylated H3K36 in transcriptionally active chromatin.

INTRODUCTION

Many post-translational modifications on histone proteins are essential for processes in the underlying chromatin. Typically, histone modifications themselves do not alter chromatin structure directly but function by binding effector proteins which alter chromatin or by interfering with such interactions. The histone methyltransferase Polycomb Repressive Complex 2 (PRC2) and its regulation by accessory proteins and histone modifications represent a prime example for understanding these interaction mechanisms (Laugesen et al., 2019; Yu et al., 2019). PRC2 trimethylates lysine 27 in histone H3 (H3K27me3), a modification that is essential for the transcriptional repression of developmental regulator genes that control cell fate decisions in metazoans (McKay et al., 2015; Pengelly et al., 2013). H3K27me3 marks chromatin for interaction with PRC1, an effector which compacts chromatin (Francis et al., 2004; Grau et al., 2011). H3K27me3 is also recognized by PRC2 itself, and this interaction allosterically activates the PRC2 enzyme complex to facilitate deposition of H3K27me3 across

52 extended domains of chromatin (Hansen et al., 2008; Jiao and Liu, 2015; Margueron et al.,
53 2009). Genetic studies and subsequent biochemical work established that PRC2 is in addition
54 subject to negative regulation. In particular, the H3K4me3, H3K36me2 and H3K36me3 marks
55 present on nucleosomes in transcriptionally active chromatin directly inhibit H3K27
56 methylation by PRC2 (Gaydos et al., 2012; Klymenko and Müller, 2004; Schmitges et al., 2011;
57 Streubel et al., 2018; Yuan et al., 2011). Importantly, while stimulation of PRC2 activity by
58 H3K27me3 acts *in trans*, inhibition of PRC2 by H3K4me3, H3K36me2 and H3K36me3
59 requires that these modifications are present *in cis*, that is, on the same H3 molecule containing
60 the K27 substrate lysine (Schmitges et al., 2011; Yuan et al., 2011). While recent structural
61 studies have uncovered the allosteric activation mechanism for PRC2 (Jiao and Liu, 2015;
62 Justin et al., 2016), the molecular basis of PRC2 inhibition by active chromatin marks has
63 remained enigmatic. In particular, in nucleosome binding assays, PRC2-DNA interactions
64 make the largest contribution to the nucleosome-binding affinity of PRC2 (Choi et al., 2017;
65 Wang et al., 2017) and H3K4me3, H3K36me2 and H3K36me3 do not seem to have a major
66 effect on this binding affinity (Guidotti et al., 2019; Jani et al., 2019; Schmitges et al., 2011).
67 Instead, these three modification were found to reduce the k_{cat} of PRC2 for H3K27 methylation
68 (Jani et al., 2019; Schmitges et al., 2011). Recent cross-linking studies led to the suggestion of
69 a possible sensing pocket for H3K36 on the surface of EZH2 (Jani et al., 2019) but there is no
70 structural data how that proposed interaction might occur. Similarly, a recent structure of PRC2
71 bound to a dinucleosome revealed how the catalytic lobe of PRC2 contacts nucleosomes
72 through DNA interactions but provided no structural insight into how the H3 N-termini might
73 be recognized (Poepsel et al., 2018). Here, a refined structure of PRC2 bound to a
74 dinucleosome allowed us to visualize how the histone H3 N-terminus on substrate nucleosomes
75 is threaded into the EZH2 active site. Our analyses reveal that H3K36 assumes a critical
76 position in the PRC2-nucleosome interaction interface that permits the complex to gauge the
77 H3K36 methylation state.
78
79

80 **RESULTS**

81 **EZH2 interaction with nucleosomal DNA orients the H3 N-terminus for H3K27 binding**
82 **to the active site**

83 We assembled recombinant full-length human PRC2 in complex with its accessory factor PHF1
84 (i.e. PHF1-PRC2) (Choi et al., 2017) on a heterodimeric dinucleosome (di-Nuc), which
85 consisted of a 'substrate' nucleosome with unmodified histone H3 and an 'allosteric'
86 nucleosome containing H3 with a trimethyllysine analog (Simon et al., 2007) at K27, separated
87 by a 35 base pair (bp) DNA linker (Poepsel et al., 2018) (**Figure 1A, B**). Single particle cryo-
88 electron microscopy analysis yielded a reconstruction of the PHF1-PRC2:di-Nuc assembly
89 with an overall resolution of 5.2 Å (**Supplementary Figures 1-3**). The map showed clear
90 density for the catalytic lobe of PRC2 with similar chromatin interactions and binding geometry
91 as previously described for the catalytic lobe of AEBP2-PRC2 (Poepsel et al., 2018) where
92 PRC2 contacts the two nucleosomes via interactions with the DNA gyres (**Figure 1C**).
93 Specifically, the substrate nucleosome is bound by the $EZH2_{CXC}$ domain residues K563, Q565,
94 K569 and Q570 (**Figure 1D, Supplementary Figure 4A**, cf. (Poepsel et al., 2018)), while the
95 allosteric nucleosome is contacted by EED and by the SBD and SANT1 domains of EZH2
96 (**Figure 1E**, cf. (Poepsel et al., 2018)). We could not detect density for the 'bottom lobe' of
97 PRC2 (Chen et al., 2018; Kasinath et al., 2018) or for the N-terminal winged-helix and tudor
98 domains of PHF1 that bind DNA and H3K36me3, respectively (Ballaré et al., 2012; Cai et al.,
99 2013; Choi et al., 2017; Li et al., 2017; Musselman et al., 2013).

100 Using particle signal subtraction and focused refinement on the interface of EZH2 and
101 the substrate nucleosome (**Supplementary Figures 2-3**), we then obtained an improved map
102 at an apparent overall resolution of 4.4 Å which revealed well-defined density for the H3 N-
103 terminus (**Figure 1F, Supplementary Figure 3B-D**). The visible sidechain density combined
104 with the crystallographic models of the PRC2 catalytic lobe and of the mononucleosome
105 enabled us to build a pseudo-atomic model of the histone H3 N-terminus spanning residues
106 R26 to K37 (**Figure 1F**). This model revealed that EZH2 recognizes the H3 N-terminus via an
107 extended network of contacts besides the previously described ionic interactions near the active

site where H3 R26 interacts with EZH2 Q648/D652, and H3 K27 with the aromatic cage above the EZH2 catalytic center (Justin et al., 2016) (**Figure 1F**). Specifically, our structure suggests two hydrophobic hotspots, the first one involving H3 A29/P30 and EZH2 residues F667, A697, V699, I708 and F724 and the second one involving H3 V35 and F542, F557 and P558 of EZH2 (**Figure 1F**). H3 G33/G34 is likely not recognized by PRC2 but might act as a flexible hinge between the two hydrophobic interaction sites (**Figure 1F**). H3K36 is directly juxtaposed to the $EZH2_{CXC}$-DNA interaction surface and appears to be involved in the EHZ2-DNA interface. The side chain density of H3K36 suggests that the epsilon-amino group of H3K36 engages in a polar interaction with the carbonyl group of Q570 and in long-range electrostatic interactions with the phosphate backbone of the nucleosomal DNA (**Figure 1F, Supplementary Figure 4 C-E**). Taken together, our analyses reveal that an extensive network of interactions between EZH2, the nucleosomal DNA and the H3 N-terminus. This complex geometric arrangement orients the H3 N-terminus into an extended conformation, threading H3K27 into the EZH2 active site. In this context, it should be noted that a previously postulated H3K36-binding pocket centered on E579 of EZH2 (Jani et al., 2019) is located approximately 19 Å away from H3K36 in our structure (**Supplementary Figure 4F**). An interaction of H3K36 with E579 of EZH2 as proposed by Muir and co-workers (Jani et al., 2019) would require a very different binding geometry of PRC2 on the nucleosome and major structural rearrangements of PRC2 or the nucleosome in order to avoid steric clashes.

The EZH2 CXC contact with DNA is essential for H3K27 methylation

We next analysed how the PRC2 surfaces contacting the substrate and the allosteric nucleosome contribute to the formation of productive PRC2-chromatin interactions. For these experiments, we used $PHF1_C$-PRC2, which contains the minimal 5-kDa PRC2-interaction domain of PHF1 (**Figure 1A**, (Chen et al., 2020; Choi et al., 2017)) but lacks the H3K36me3-binding tudor and the DNA-binding winged-helix domains of PHF1 (Choi et al., 2017; Li et al., 2017; Musselman et al., 2013). $PHF1_C$-PRC2 therefore only retains the DNA-binding surfaces of the 4-subunit PRC2 core complex and was used because it generally behaved better in purifications than the

136 4-subunit PRC2 core complex. For simplicity we shall, in the following, refer to the PHF1$_C$-
137 PRC2 complex as PRC2. We generated three mutant versions of PRC2. In PRC2$^{CXC>A}$ (K563A
138 Q565A K569A Q570A), the EZH2$_{CXC}$ interface is mutated (**Figure 1D**), in PRC2$^{EED>A}$ (K77A
139 K83A K385A K398A K400A K408A), the EED interface contacting the allosteric nucleosome
140 (**Figure 1E**), is mutated, and PRC2$^{CXC>A/EED>A}$ carries the combination of these mutations. We
141 first used electromobility shift assays (EMSA) to measure the binding affinity of wild-type and
142 mutant PRC2 complexes on mononucleosomes. These mononucleosomes were assembled on
143 a 215 bp long DNA fragment containing the 147-bp 601 nucleosome-positioning sequence
144 (Lowary and Widom, 1998) in the center and linker DNA on both sides. Wild-type PRC2
145 bound this mononucleosome with an apparent K_d in the mid-nanomolar range (**Figure 2A, B**,
146 cf. (Choi et al., 2017)). The binding affinities of PRC2$^{CXC>A}$ or PRC2$^{EED>A}$ were two- to three-
147 fold lower than that of wild-type PRC2 and that of PRC2$^{CXC>A/EED>A}$ was about five-fold lower
148 compared to the wild-type complex (**Figure 2A, B**, compare lanes 11-30 with 1-10, and
149 **Supplementary Figure 5A**). The residual nucleosome binding shown by PRC2$^{CXC>A/EED>A}$
150 (**Figure 2A**, lanes 21-30) could in part be due to incomplete disruption of the mutated interfaces
151 but in part is likely also due to the previously identified nucleosome-binding activity of the
152 PRC2 bottom lobe (Chen et al., 2018; Nekrasov et al., 2005). The overall binding affinity of
153 the PRC2 core complex for chromatin therefore appears to result from interactions of at least
154 three distinct surfaces of this complex with nucleosomes. Among those, binding of the
155 EZH2$_{CXC}$ domain to the nucleosomal DNA contributes only modestly to the total binding
156 affinity.

157 We then analysed the histone methyltransferase (HMTase) activity of PRC2$^{CXC>A}$. On
158 the same mononucleosomes used above, PRC2$^{CXC>A}$ showed almost no detectable HMTase
159 activity compared to wild-type PRC2 (**Figure 2C**, compare lanes 5-7 with 2-4, see also
160 **Supplementary Figure 5B**). On dinucleosomes, EED binding to one nucleosome might be
161 expected to facilitate interaction of the mutated EZH2$^{CXC>A}$ domain with the H3 N-termini on
162 the juxtaposed second nucleosome. Indeed, on dinucleosomes, the PRC2$^{CXC>A}$ complex does
163 generate H3K27me1 and -me3 but less efficiently than wild-type PRC2 (**Figure 2C**, compare

164 lanes 12-14 with 9-11). When comparing the activities of the different complexes, it should be
165 kept in mind that the interpretation of H3K27me3 formation as read-out of complex activity on
166 dinucleosomes is more complicated than on mononucleosomes, because H3K27me3, once
167 placed on one of the nucleosomes, will allosterically activate PRC2 to methylate H3K27 on the
168 linked second nucleosome (Margueron et al., 2009) (Jiao and Liu, 2015). The main conclusion
169 to be drawn from our analyses here is that the DNA-binding interaction of the $EZH2_{CXC}$ domain
170 with substrate nucleosomes is critical for engaging the H3 N-terminus in a manner that allows
171 H3K27 methylation.
172
173 **Unmodified H3K36 in the $EZH2_{CXC}$-DNA interaction interface is critical for H3K27**
174 **methylation in nucleosomes**
175 The architecture of the $EZH2_{CXC}$-DNA interface around H3K36 (**Figure 1F**) suggested that a
176 bulkier side chain, such as that of a tri- or di-methylated lysine or an arginine may not be
177 accommodated in this interface. In EMSAs, the affinity of PRC2 for binding to
178 mononucleosomes containing a trimethyllysine analog at H3K36 (H3Kc36me3) was
179 indistinguishable from that for binding to unmodified mononucleosomes (**Figure 3A, B**).
180 However, as previously reported (Schmitges et al., 2011; Yuan et al., 2011), H3K27 mono- and
181 trimethylation by PRC2 was strongly inhibited on H3Kc36me3-containing mononucleosomes
182 (**Figure 3C**, compare lanes 5-7 with 2-4, see also **Supplementary Figure 6A**). Methylation of
183 H3K27 was also inhibited on mononucleosomes where H3K36 had been mutated to arginine
184 or alanine ($H3^{K36R}$ and $H3^{K36A}$ mononucleosomes, respectively) (**Figure 3C**, compare lanes 8-
185 13 with 2-4). PRC2 inhibition on $H3^{K36R}$ and $H3^{K36A}$ mononucleosomes was, however, less
186 severe than on H3Kc36me3 mononucleosomes (**Figure 3C**, compare lanes 8-13 with 5-7). We
187 note that the quantitative analyses here show inhibition of PRC2 HMTase activity on $H3^{K36A}$
188 mononucleosomes, consistent with earlier studies (Jani et al., 2019), whereas other studies
189 previously had failed to detect inhibition on $H3^{K36A}$ mononucleosomes (Schmitges et al., 2011).
190 Taken together, our structural and biochemical analyses suggest that the unmodified side chain
191 of H3K36 is critical for the productive positioning of H3K27 in the catalytic center of PRC2.

192 Neither the bulkier side chains of trimethyllysine or arginine nor the short apolar side chain of
193 alanine appear to provide the correct fit at the position of H3K36. Finally, we compared PRC2
194 HMTase activity on histone $H3_{18-42}$ peptides that were either unmodified or contained
195 H3K36me3 using a Masspectrometry-based methylation assay. Importantly, on this isolated
196 peptide, H3K36me3 did not inhibit H3K27 monomethylation by PRC2 (**Figure 3D,**
197 **Supplementary Figure 6B**). The allosteric inhibition of PRC2 by H3K36me3 therefore only
198 occurs in the context of the geometric constraints of the nucleosome.
199
200 **H3K36me3 inhibits H3K27 methylation by PHF1-PRC2**
201 DNA-binding by the winged-helix domain of PHF1 increases the binding affinity and residence
202 time of PHF1-PRC2 on nucleosomes about two- to three-fold, resulting in more efficient
203 H3K27 methylation by this complex compared to PRC2 (Choi et al., 2017). Furthermore, the
204 PHF1 tudor domain binds to H3K36me3 in the context of a nucleosome (Musselman et al.,
205 2013). To investigate whether these interactions might modulate PRC2 inhibition by
206 H3K36me3, we compared the HMTase activity of full-length PHF1-PRC2 (**Figure 1B**) on
207 unmodified and H3Kc36me3 mononucleosomes. H3K27 mono- and tri-methylation by PHF1-
208 PRC2 was strongly inhibited on H3Kc36me3 mononucleosomes (**Supplementary Figure 6C**).
209 H3K36me3 therefore inhibits H3K27 methylation by PHF1-PRC2 even though this complex
210 has higher binding-affinity and a prolonged residence time on nucleosomes (Choi et al., 2017).
211 Further analyses will be needed to assess whether and how interaction of the PHF1 tudor
212 domain with H3K36me3 might change H3K27 methylation by PHF1-PRC2 on more complex
213 oligonucleosome substrates containing H3K36me3- and unmodified nucleosomes.
214
215 ***Drosophila* with $H3^{K36R}$ or $H3^{K36A}$ mutant chromatin arrest development at different**
216 **stages**
217 The observation that PRC2 is not only inhibited on H3K36me2/3-modified nucleosomes but
218 also on $H3^{K36R}$ and on $H3^{K36A}$ mutant nucleosomes prompted us to investigate how H3K27
219 trimethylation is affected in *Drosophila* with $H3^{K36R}$ or $H3^{K36A}$ mutant chromatin. H3K27me3

220 is primarily found on canonical histone H3 (McKay et al., 2015; Pengelly et al., 2013). We
221 used the following strategy to replace the canonical histone H3 gene copies encoded in the *HisC*
222 gene cluster with $H3^{K36R}$ or $H3^{K36A}$ mutant versions. Animals that are homozygous for a
223 deletion of the *HisC* gene cluster (i.e. *Df(2L)HisC* homozygotes) arrest development at the
224 blastoderm stage after exhaustion of the pool of maternally-deposited histones but transgene
225 cassettes providing 12 copies of the wild-type histone gene unit ($12xHisGU^{WT}$) rescue
226 *Df(2L)HisC* homozygotes into viable adults (Günesdogan et al., 2010; McKay et al., 2015).
227 We therefore generated *Df(2L)HisC* homozygotes carrying $12xHisGU^{H3K36R}$ or $12xHisGU^{H3K36A}$
228 transgene cassettes and shall refer to these animals as $H3^{K36R}$ and $H3^{K36A}$ mutants, respectively.
229 The *Drosophila* strains to generate $H3^{K36R}$ mutant animals had been described previously
230 (McKay et al., 2015). The strain for generating $H3^{K36A}$ mutants was constructed in this study.
231 $H3^{K36R}$ mutant animals complete embryogenesis and their cuticle morphology is
232 indistinguishable from wildtype (**Supplementary Figure 7**). In agreement with the results
233 from Matera and colleagues (McKay et al., 2015), we found that these animals arrest
234 development during the larval or pupal stages. Specifically, 81% of $H3^{K36R}$ mutant animals
235 arrested development at variable time points during larval growth, 18% develop to form pupae
236 that die prior to metamorphosis, and 1% develop into late pupae that complete metamorphosis
237 but then arrest as pharate adults (**Supplementary Figure 7**). Like Matera and colleagues
238 (McKay et al., 2015), we have not observed any $H3^{K36R}$ mutants that eclose from the pupal case,
239 and both our studies therefore disagree with a report from the Schwartz lab who claimed that
240 $H3^{K36R}$ mutants would be able to develop into adults (Dorafshan et al., 2019). When we
241 dissected the rare $H3^{K36R}$ mutant pharate adults from their pupal cases and examined their
242 epidermal structures, we found that they consistently showed homeotic transformations
243 reminiscent of Polycomb group (PcG) mutants. These PcG mutant phenotypes included
244 antenna-to-leg transformations and extra sex comb teeth on meso- and metathoracic legs in
245 males (**Supplementary Figure 7**). A molecular analysis of these PcG phenotypes will be
246 presented below.

247 *H3^{K36A}* mutants also complete embryogenesis and the morphology of their embryonic
248 cuticle also appeared indistinguishable from wildtype (**Supplementary Figure 7**). 96% of the
249 *H3^{K36A}* mutant animals arrest development before hatching from the eggshell and the 4% that
250 hatch die during the first larval instar (**Supplementary Figure 7**). *H3^{K36A}* mutants therefore
251 arrest development earlier and in a narrower time window than *H3^{K36R}* mutants. The molecular
252 basis for the earlier lethality of *H3^{K36R}* mutant animals remains to be determined. However, it
253 is not unusual that mutations changing the chemical properties of a particular histone lysine
254 residue result in phenotypes with different severity (e.g. (Copur et al., 2018))
255
256 ***Drosophila* with H3^{K36R} or H3^{K36A} mutant chromatin show diminished H3K27me3 levels**
257 **at canonical PcG target genes**
258 We next performed Western blot analyses to examine H3K36me2, H3K36me3 and H3K27me3
259 bulk levels in *H3^{K36R}* and *H3^{K36A}* mutant animals. In the case of *H3^{K36R}* mutants, we used
260 extracts from diploid imaginal disc and central nervous system (CNS) tissues dissected from
261 third instar larvae, and in the case of *H3^{K36A}* mutants we used total nuclear extracts from late-
262 stage embryos. For the interpretation of the following experiments, it is important to keep in
263 mind that *H3^{K36R}* and *H3^{K36A}* zygotic mutant animals initially also contain a pool of maternally-
264 deposited wild-type canonical H3 molecules that, together with H3^{K36R} and H3^{K36A}, become
265 incorporated into chromatin during the pre-blastoderm cleavage cycles. Even though these
266 wild-type H3 molecules then become diluted during every cell cycle and are eventually fully
267 replaced by mutant H3, they are probably still present in the chromatin of late-stage embryos
268 because of the few cell divisions that take place prior to the end of embryogenesis. In diploid
269 tissues from larvae, replacement by mutant H3 is expected to be much more complete because
270 of the extensive cell proliferation that occurs in these tissues during larval growth.
271 In *H3^{K36R}* mutant larvae, H3K36me2 and H3K36me3 bulk levels were reduced more
272 than 4-fold compared to wildtype (**Figure 4A**). The residual H3K36me2 and H3K36me3
273 signals (**Figure 4A**, lane 4) probably represent the methylated versions of the histone variant
274 H3.3 that are encoded by the genes *H3.3A* and *H3.3B* that are not located in the *HisC* locus and

275 had not been mutated in these animals. Intriguingly, *H3*^{K36R} mutant animals also showed an
276 about two-fold reduction in H3K27me3 bulk levels compared to wildtype (**Figure 4A**, compare
277 lanes 4-6 with 1-3). The reduction of not only H3K36me2 and H3K36me3 but also of
278 H3K27me3 bulk levels in *H3*^{K36R} mutant larvae was previously also noted by Matera and
279 colleages (Meers et al., 2017). H3K27 tri-methylation by PRC2 therefore appears to be
280 compromised in *Drosophila* chromatin consisting of H3^{K36R} nucleosomes.

281 In *H3*^{K36A} mutant embryos, H3K36me2 and H3K36me3 bulk levels were reduced about
282 3- to 4-fold comprared to wildtype (**Figure 4B**, compare lanes 5-8 with 1-4). Part of the residual
283 H3K36me2 and H3K36me3 methylation signals in *H3*^{K36A} mutant embryos probably represents
284 the methylated versions of the histone variant H3.3. However, considering that the reduction
285 is less pronounced than in *H3*^{K36R} mutant larvae, at least some of the H3K36me2 and
286 H3K36me3 signal might also represent maternally-deposited wild-type canonical H3.
287 H3K27me3 bulk levels appeared largely unchanged compared to wildtype (**Figure 4B**,
288 compare lanes 5-8 with 1-4).

289 We next performed ChIP-seq experiments to examine how the genome-wide profiles
290 of H3K36me2 and H3K27me3 are changed in *H3*^{K36R} and *H3*^{K36A} mutants. In the case of *H3*^{K36R}
291 mutants, we compared these profiles in cells from imaginal disc and CNS tissues dissected from
292 late-stage third instar *H3*^{K36R} and wildtype larvae, and in the case of *H3*^{K36A} mutants we
293 compared the profiles in late-stage *H3*^{K36A} and wildtype embryos. As expected from the
294 Western blot analyses (**Figure 4A, B**), H3K36me2 levels across the genome were strongly
295 diminished, both in *H3*^{K36R} mutant larvae and in *H3*^{K36A} mutant embryos (**Figure 4C-F,**
296 **Supplementary Figure 8, Table S2**). The H3K27me3 profiles confirmed that the levels of
297 this modification were reduced in *H3*^{K36R} mutant larvae (**Figure 4C**). While the average
298 reduction was only about two-fold, H3K27me3 levels were particularly strongly diminished at
299 canonical PRC2 target genes such as the HOX genes that in wildtype animals are decorated
300 with high-levels of H3K27me3 (**Figure 4C, E, Supplementary Figure 8, Table S2**).
301 Specifically, at the HOX genes *Ultrabithorax* (*Ubx*), *abdominal-A* (*abd-A*), *Abdominal-B* (*Abd-*
302 *B*) or *Antennapedia* (*Antp*), H3K27me3 levels in *H3*^{K36R} mutants were between 3- and 4-fold

303 lower than in wildtype (**Figure 4C, E**). As expected from the Western blot analyses (**Figure**
304 **4B**), *H3*^{K36A} mutant embryos did not show a general reduction in the H3K27me3 profile (**Figure**
305 **4D**). However, H3K27me3 levels were 1,5-fold reduced across the HOX genes (**Figure 4D,**
306 **F**). In *Drosophila* with H3^{K36R} or H3^{K36A} chromatin, PRC2 therefore appears to be unable to
307 generate high levels of H3K27me3 at Polycomb target genes.
308

309 **Polycomb repression of HOX genes is impaired in *Drosophila* with H3^{K36R} or H3^{K36A}**
310 **mutant chromatin**

311 The PcG-like phenotypes in the rare *H3*^{K36R} mutant animals that survive into pharate adults and
312 the reduction of H3K27me3 levels at HOX genes in these mutants prompted us to analyse
313 whether and how expression of these genes is altered in *H3*^{K36R} and *H3*^{K36A} mutants. In a first
314 set of experiments, we analysed HOX gene expression in embryos. Both mutants showed
315 stochastic misexpression of *Abd-B* in single cells in late stage embryos (**Figure 5A**). *Abd-B*
316 misexpression in *H3*^{K36R} and *H3*^{K36A} mutant embryos was however clearly less widespread than
317 in *H3*^{K27R} mutant embryos or in embryos lacking the PRC2 subunit Esc that are shown for
318 comparison (**Figure 5A**). Moreover, we were unable to detect misexpression of *Antp* or *Ubx*
319 in *H3*^{K36R} or *H3*^{K36A} mutant embryos.

320 We next analysed HOX gene expression in imaginal discs and CNS tissues from third
321 instar *H3*^{K36R} mutant larvae. In the CNS of every single mutant individual, *Ubx* was widely
322 misexpressed in many single cells in an apparently stochastic pattern (**Figure 5B**). 50% of the
323 *H3*^{K36R} mutant larvae also showed stochastic misexpression of *Ubx* in individual cells in the
324 wing pouch of the wing imaginal disc (**Figure 5C**). *Ubx* misexpression in *H3*^{K36R} mutant wing
325 discs was less widespread than in *H3*^{K27R} mutants that are shown for comparison (**Figure 5C**).
326 Finally, we found that 100% of the *H3*^{K36R} mutant larvae showed misexpression of *Antp* in the
327 antenna primordium of the eye-anntennal disc (**Figure 5D**). We also observed this
328 misexpression in clones of *H3*^{K36A} homozygous cells that we had induced in *H3*^{K36A}
329 heterozygous animals (**Figure 5D**) and in *H3*^{K27R} mutant clones that were induced as control
330 (**Figure 5D**). *Drosophila* with chromatin consisting of *H3*^{K36R} or *H3*^{K36A} nucleosomes therefore

331 show stochastic misexpression of multiple HOX genes. The most straightforward interpretation
332 of this misexpression is that it is caused by defective Polycomb repression as a result of the
333 reduced H3K27me3 levels in HOX gene chromatin.
334
335
336 **DISCUSSION**
337 Understanding how PRC2 binds chromatin and how it is regulated is essential for understanding
338 how the complex marks genes for Polycomb repression to maintain cell fate decisions. The
339 work in this study leads to the following main conclusions. First, the structure of nucleosome-
340 bound PHF1-PRC2 allowed to visualize how interaction of the catalytic lobe of the complex
341 with the substrate nucleosome threads the histone H3 N-terminus into the active site of EZH2
342 through a relay of contacts. Second, structure-guided mutational analyses showed that DNA-
343 binding by the $EZH2_{CXC}$ domain is critical for productive PRC2-nuclesome interactions. Third,
344 unmodified H3K36 is accommodated in a key position in the $EZH2_{CXC}$-DNA interface and
345 while H3K36 provides the correct fit, the methylated forms H3K36me2/3, or mutated H3K36R
346 or H3K36A do not seem to fit because they strongly diminish H3K27 methylation. Fourth,
347 H3K36 is also critical for normal H3K27 methylation *in vivo* because *Drosophila* with $H3^{K36R}$
348 or $H3^{K36A}$ mutant chromatin show reduced levels of H3K27me3 and fail to fully maintain
349 Polycomb repression at HOX target genes. In the following, we shall discuss key aspects of
350 these new findings in the context of our previous knowledge of PRC2 regulation and function.
351
352 **Different forms of PRC2 use the same molecular interactions for binding the H3 N-**
353 **terminus on substrate nucleosomes**
354 Unlike many other histone-modifying enzymes (e.g. (McGinty et al., 2014; Worden et al.,
355 2019)), PRC2 does not recognize the nucleosome by docking on its acidic patch (Luger et al.,
356 1997) to engage with the histone substrate. Instead, the complex interacts with chromatin by
357 binding to the DNA gyres on the nucleosome ((Poepsel et al., 2018), this study). Prevous
358 studies that had measured the binding affinity and residence time of PRC2 on nucleosomes and

359 free DNA had found that DNA-binding makes the largest make contribution to the chromatin-
360 binding affinity of PRC2 (Choi et al., 2017; Wang et al., 2017). The mutational analyses here
361 establish that interaction of highly conserved residues in the $EZH2_{CXC}$ domain with the DNA
362 on the substrate nucleosome is critical for H3K27 methylation (**Figure 2C**). Moreover, this
363 interaction sets the register for a network of interactions of the H3 N-terminus with the EZH2
364 surface that permits H3K27 to reach into the active site (**Figure 1 D, F**). Consistent with our
365 findings here, an independent recent study of a cryo-EM structure of PRC2 with co-factors
366 JARID2 and AEBP2 bound to a mononucleosome with monoubiquitylated H2A (Kasinath et
367 al., 2020) identified very similar interactions of EZH2 with the nucleosomal DNA and the H3
368 N-terminus. Different forms of PRC2 that contain different accessory proteins and dock in
369 different ways on chromatin therefore contact the substrate H3 N-terminus in the nuclesosome
370 through similar interactions.
371
372 **The position of H3K36 in the $EZH2_{CXC}$-nucleosome interface enables allosteric regulation**
373 **by H3K36 methylation**
374 Important novel insight from our structure came from the observation that unmodified H3K36
375 is located in a critical position in the $EZH2_{CXC}$-DNA interface. Unmodified H3K36 has the
376 right fit for interaction of the H3 N-terminus with the EZH2 surface and placement of H3K27
377 in the active site. The inhibition of H3K27 mono-, di- and tri-methylation on nucleosomes
378 carrying H3K36me2 or -me3 (Schmitges et al., 2011; Yuan et al., 2011) or on $H3^{K36R}$ or $H3^{K36A}$
379 nucleosomes (**Figure 3C**) suggests that these alterations of the H3K36 side chain impair the
380 interaction of H3K27 with the active site of EZH2. On isolated H3 N-terminal peptides,
381 H3K36me3 did not inhibit the formation of H3K27me1 (**Figure 3D**), consistent with earlier
382 findings that on peptide substrates H3K36me3 only has a minor effect on the kcat of H3K27
383 methylation (Schmitges et al., 2011) (Jani et al., 2019). Also, H3K36me3 does not diminish
384 the affinity of PRC2 for binding to mononucleosomes (**Figure 3A, B**) and does not reduce the
385 residence time of PRC2 on nucleosome arrays (Guidotti et al., 2019). Taken together, a possible
386 scenario would therefore be that within the time frame of the PRC2 nucleosome binding and

387 reaction cycle, docking of the H3K36 side chain in the EZH2$_{CXC}$-DNA interface is critical for
388 rapid alignment of the H3 N-terminus on the EZH2 surface into a catalytically competent state.
389 According to this view, H3K36me2/3 does not locally disrupt nucleosome binding but
390 allosterically inhibits H3K27 from interacting with the EZH2 active site.
391

392 **H3K27 methylation and Polycomb repression are defective in Drosophila with H3^{K36R} or**
393 **H3^{K36A} chromatin**

394 The finding that PRC2 is inhibited on H3^{K36R} and H3^{K36A} nucleosomes *in vitro* had prompted
395 us to use a genetic histone replacement strategy in *Drosophila* (Günesdogan et al., 2010)
396 (McKay et al., 2015) to assess PRC2 inhibition on H3^{K36R} or H3^{K36A} chromatin *in vivo*. Previous
397 studies had found that *Drosophila H3^{K36R}* mutants are able to develop into the pupal stages and,
398 consistent with this late develpomental arrest, whole third instar larvae were found to show only
399 relatively minor changes in their transriptome compared to wildtype animals (McKay et al.,
400 2015; Meers et al., 2017). Here, we found that a few rare *H3^{K36R}* mutant animals even survive
401 into pharate adults and that these show remarkably little morphological defects apart from
402 homeotic transformations characteristic of Polycomb mutants (**Figure S7**). We show that these
403 phenotypes are caused by defective Polycomb repression of multiple HOX genes (**Figure 5**)
404 and that they are linked to reduced levels of H3K27me3 at these genes (**Figure 4**). A simple
405 straightforward explanation for these phenotypes in *H3^{K36R}* or *H3^{K36A}* mutant animals is that
406 PRC2 is unable to effectively deposit high levels of H3K27me3 on the H3^{K36R} or H3^{K36A}
407 nucleosomes, respectively, in their chromatin. Accordingly, H3K27me3 levels at HOX genes
408 are below the threshold needed to reliably maintain Polycomb repression and consequently,
409 HOX genes become stochastically misexpressed in a fraction of cells. Finally, we note that in
410 *H3^{K36R}* mutant larvae, the experimental setting where we have been able to generate the most
411 complete replacement of H3 by H3^{K36R}, H3K27me3 levels at HOX genes were only about 3- to
412 4-fold reduced compared to wildtype (**Figure 4C**). However, as shown in **Figure 3C**, on
413 nucleosomes *in vitro*, H3K36me3 inhibited PRC2 more effectively than H3^{K36R} or H3^{K36A}. It
414 therefore seems likely that in contrast to the *H3^{K36R}* and *H3^{K36A}* mutants that we have used as

415 proxy, H3K36me2 and H3K36me3 *in vivo* also inhibit PRC2 more effectively from depositing
416 H3K27me3 on H3K36me2- or H3K36me3-modified nucleosomes in transcriptionally active
417 chromatin.
418
419 **Concluding remark**
420 The structural, biochemical and genetic work reported in this study shows that it is the exquisite
421 geometry formed by a relay of interactions between the PRC2 enzyme, nucleosomal DNA and
422 the H3 N-terminus that enable the histone methylation marks H3K36me2 and H3K36me3 in
423 transcriptionally active chromatin to allosterically prevent PRC2 from depositing the repressive
424 histone methylation mark H3K27me3 at transcribed genes.
425
426
427 **MATERIALS AND METHODS**
428
429 Protein expression and purification
430 Human PHF1-PRC2 wild-type (wt) complex was expressed and purified as previously
431 described (Choi et al., 2017). In brief, an optimized ratio of the baculoviruses for the different
432 PHF1-PRC2 subunits was used to infect HiFive cells (Invitrogen). Cell were lysed using a glass
433 Dounce homogenizer and the complex was purified using affinity chromatography (Ni-NTA
434 and Strep-tag), followed by simultaneous TEV mediated protease tag cleavage and Lambda
435 Phosphatase treatment (obtained from the MPI of Biochemistry Protein Core facility) and a
436 final size exclusion chromatography (SEC) step in a buffer containing 25 mM Hepes, pH 7.8,
437 150 mM NaCl, 10% glycerol, 2 mM DTT.
438 $PRC2^{CXC>A}$, $PRC2^{EED>A}$ and $PRC2^{CXC>A/EED>A}$ mutants were generated by PCR with primers
439 containing the desired mutations, subsequent ligation and transformation. Expression and
440 purification were performed as above.
441 *Xenopus laevis* (*X.l.*) and *Drosophila melanogaster* (*D.m.*) histones were expressed and purified
442 from inclusion bodies as described in (Luger et al., 1999). To mimic the inhibitory mark
443 H3K36me3 or the allosteric activating mark H3K27me3, the cysteine side chain of a mutated
444 *D.m.* histone $H3^{C110A\ K36C}$ or *X.l.* histone $H3^{C110A\ K27C}$ was alkylated with (2-bromoethyl)
445 trimethylammonium bromide (Sigma Aldrich) as described previously (Simon et al., 2007).
446 Nucleosomes containing these modifications are abbreviated with e.g. H3Kc36me3.
447
448 For histone octamers, equimolar amounts of histones H2A, H2B, H4 and H3 (wt, $H3^{K36A}$,
449 $H3^{K36R}$, H3Kc27me3 or H3Kc36me3) were mixed and assembled into octamers in high salt
450 buffer containing 10 mM Tris-HCL pH 7.5, 2 M NaCl, 1 mM EDTA, 5 mM β-mercaptoethanol.
451 Subsequent SEC was performed to separate octamers from H3/H4 tetramers or H2A/H2B
452 dimers (Luger et al., 1999).
453
454 Reconstitution of nucleosomes:
455 For *X.l.* and *D.m* mononucleosomes used in biochemical assays, 6-carboxyfluorescein (6-FAM)-
456 labeled 215 bp 601 DNA (Lowary and Widom, 1998) was PCR amplified from the p601

plasmid, purified on a MonoQ column (GE Healthcare), precipitated with ethanol and dissolved in the same high salt buffer used for octamers. Optimized ratios of octamer to DNA (usually ranging between 0.8-1.3 : 1) were mixed and nucleosomes were reconstituted by gradient and stepwise dialysis against low salt buffers to a final buffer containing 25 mM Hepes, pH 7.8, 60 mM NaCl, 2 mM DTT.

X.l. asymmetrical dinucleosomes for cryo-EM studies containing one unmodified substrate nucleosome and one H3K27me3-modified (allosteric) nucleosome connected with a 35 bp linker DNA were reconstituted using the protocol described in (Poepsel et al., 2018). In brief, substrate nucleosomes and allosteric nucleosomes were separately assembled on the respective *DraIII* digested nucleosomal DNA. The latter was generated by PCR with primers introducing the desired linker and *DraIII* recognition sites and purified as described above. The assembled nucleosomes were purified on a preparative native gel system (Biorad 491 prep cell). After ligation using T4 ligase (Thermo Fisher Scientific) the resulting dinucleosomes were purified from aberrant or non-ligated mononucleosomes by a second preparative native gel system (Biorad 491 prep cell). In contrast to (Poepsel et al., 2018), the dinucleosome DNA used in this study contained an additional 30 bp overhang on the substrate nucleosome, thus resulting in the following DNA sequence:

5′–601 binding (allosteric nucleosome) – agcgatctCACCCCGTGatgctcgatactgtcata – 601 binding (substrate nucleosome) – atgcatgcatatcattcgatctgagctcca –3′ (after DraIII digestion, assembly of substrate/allosteric nucleosome and ligation to dinucleosomes).

X.l. symmetrical unmodified dinucleosomes used for the HMTase assays with the PRC2^{CXC} mutants were obtained by reconstituting octamers with a 377 bp DNA containing two 601 sequences connected by a 35 bp linker DNA. A vector containing the 377 bp sequence was ordered from Invitrogen GeneArt and was used for PCR resulting in:

5′–atatctcgggcttatgtgatggac – 601 binding (substrate nucleosome 1) – agcgatctcaacgagtgatgctcgatactgtcata – 601 binding (substrate nucleosome 2) – gtattgaacagcgactcgggatat–3′.

The PCR products were purified as described above. Optimized ratios of octamer : DNA (usually ranging between 1.8-2.3 : 1) were mixed and nucleosomes were reconstituted by gradient and stepwise dialysis against low salt buffers to a final buffer containing 25 mM Hepes, pH 7.8, 60 mM NaCl, 2 mM DTT.

Cryo-EM Data acquisition

Complexes of PHF1-PRC2 and asymmetrically modified 35 bp dinucleosomes were assembled and grids were prepared as described previously, with the difference of using 0.005% NP40 instead of 0.01% (Poepsel et al., 2018). Cryo-EM data were collected on an FEI Titan Krios microscope operated at 300 kV and equipped with a post-column GIF and a K2 Summit direct detector (Gatan) operated in counting mode. A total of 3467 movies were collected at a nominal magnification of 81,000x (1.746 Å/pixel) at the specimen level using a total exposure of 53 e^- / $Å^2$ distributed over 60 frames and a target defocus range from 1.5–3 µm. Data acquisition was carried out with SerialEM.

Cryo-EM Data processing

Movies were aligned and corrected for beam-induced motion as well as dose compensated using MotionCor2 (Zheng et al., 2017). CTF estimation of the summed micrographs was performed with Gctf (Zhang, 2016) and particles were picked in Gautomatch (http://www.mrc-lmb.cam.ac.uk/kzhang/ K. Zhang, MRC LMB, Cambridge, UK) using templates created from the AEBP2-PRC2-dinucleosome cryo-EM structure (EMD-7306, (Poepsel et al., 2018). All subsequent image processing steps were performed in Relion 3.0 (Zivanov et al., 2018) as

511 shown in Fig. S2. A total of 1,028,229 candidate particles were subjected to two rounds of
512 initial 3D classification against a reference map (AEBP2-PRC2-dinucleosome low-pass filtered
513 to 60 Å) and the Bayesian fudge factor (T value) set to 8. 330,482 remaining particles were
514 subjected to two more rounds of 3D classification, this time using the best 3D model from the
515 previous run as reference. Finally, the two best 3D models were 3D refined and further
516 classified into 10 classes without translational and rotational sampling, using a T value of 4.
517 From this run, the best 3D classes with the highest nominal overall resolution and rotational
518 and translational accuracies were subjected to iterative rounds of 3D refinement, this time
519 applying a soft mask for solvent flattening, per particle CTF refinement and Bayesian polishing.
520 The highest nominal resolution was only achieved by combining several models from the
521 previous 3D run, likely due to missing particle views in one or the other individual model. The
522 final map after postprocessing had an overall nominal resolution of 5.2 Å, as determined from
523 the gold-standard FSC criterion of 0.143 (Rosenthal and Henderson, 2003) (Fig. S1D). The
524 density (Overall PHF1-PRC2:di-Nuc) with fitted models is shown in Fig.1A and in Fig. S1E
525 using UCSF ChimeraX (Goddard et al., 2018). Local resolution estimation was performed in
526 Relion 3.0 and is shown in Fig. S1B. The spherical angular distribution of all particles in the
527 final model is shown in Fig. S1C.
528 To further improve the resolution and map details of the region around the H3 N-terminus,
529 particle subtraction and focused 3D refinement was applied (Bai et al., 2015; Ilca et al., 2015;
530 Zhou et al., 2015). Using a mask generated with UCSF Chimera (Pettersen et al., 2004) and
531 Relion 3.0 the signal of the allosteric nucleosome as well as parts of PRC2 (EED and $EZH2_{allo}$)
532 was subtracted from all particle images. These signal subtracted particles were then subjected
533 to focused 3D refinement using a soft mask around the substrate nucleosome and $EZH2_{sub}$. This
534 yielded a 4.4 Å map ($EZH2_{sub}$-Nuc_{sub}) (Fig. S3B). Local resolution estimation is shown in
535 Fig.S3A. For model building and depiction, the final density was further sharpened (applied b
536 – factor: - 66) using the Multisharpen function in Coot (Emsley et al., 2010) (e.g. in Figs. 1E,
537 S3D, E and F).
538 To confirm the side chain information visible in the Coot sharpened map, Phenix Resolve
539 density modification was run on the two half maps generated from the 3D refinement of the
540 $EZH2_{sub}$-Nuc_{sub} map (Terwilliger et al., 2019). The resolution of the map according to Phenix
541 cryo EM density modification output improved to 4 Å and the resulting map was used as an
542 additional guideline for model building as well as for depiction (in Figs. S4 A-D.).
543
544 Cryo-EM data fitting, modeling and refinement
545 Available crystal structures were fitted into the final maps using rigid-body fitting in UCSF
546 Chimera and all manual remodeling, morphing and building was performed in Coot. For PRC2,
547 the crystal structure of the catalytic lobe of human PRC2 (PDB: 5HYN (Justin et al., 2016))
548 was used. Since the SBD helix and the SANT1 helix bundle of the crystal structure was not
549 accommodated well by the corresponding EM density, this region was fitted separately. A
550 model of a dinucleosome with linker DNA (Supplementary dataset 1 in (Poepsel et al., 2018),
551 including crystal structures of nucleosomes, PDB 3LZ1, also PDB 1AOI, also PDB 6T9L) was
552 fitted.
553
554 The above described overall model was then used as a starting model for fitting and building
555 $EZH2_{sub}$-Nuc_{sub} into the focused map. Where possible, missing parts in the model were built de-
556 novo, i.e. the H3 N-terminal tail (residues 30-37) between the catalytic site of PRC2 and the
557 substrate histone. Available information from crystal structures was used as a guide (PRC2 with
558 H3 peptide bound: PDB: 5HYN (Justin et al., 2016), and high resolution crystal structures of
559 nucleosomes (PDB 1AOI and PDB 6T9L) (Luger et al., 1997). Parts of $EZH2_{sub}$-Nuc_{sub} model
560 were then fitted using the morph fit routine in Coot or manually (Casañal et al., 2020).
561 Secondary structure restraints for real-space refinement were generated automatically with
562 phenix.secondary_structure_restraints (Sobolev et al., 2015) and manually curated. Hydrogens
563 were added and the model was real-space refined with a resolution- cutoff of 4.4 Å with Phenix
564 (Afonine et al., 2018) (phenix-1.18rc1-3777), using reference structures (PDB 6T9L and PDB

565 1AOI for nucleosome and one copy of the human PRC2 crystal structure generated from PDB
566 5HYN), applying strict secondary structure and Ramachandran restraints.
567 Our final model includes the modelled side chains of the fitted crystal/cryo-EM structures. This
568 is in our opinion supported by the data as the substrate nucleosome protein core is resolved to
569 app. 4 Å (Fig. S3A) and the map in these regions shows clear bulky side chain information (Fig
570 S3D). The EZH2 density is of worse quality however even at lower resolution side chains likely
571 contribute to the signal in the particle images and thereby an overall good model to map fit (in
572 our case given by the high CC values as well as $FSC_{modelvsmap}$) is arguably only ensured in the
573 presence of side chains. However we caution readers against in interpreting our model at side
574 chain resolution in poorly resolved regions.
575 Structures were visualized with UCSF ChimeraX (Goddard et al., 2018) and PyMOL2
576 (https://pymol.org/2/).
577
578 Electrophoretic mobility shift assay (EMSA)
579 EMSAs on a 1.2% agarose gel in 0.4x TBE Buffer with 45 nM 6-FAM - labeled
580 mononucleosomes (unmodified wt *X.l.* for bandshifts with the $PRC2^{CXC}$ mutants, unmodified
581 wt *D.m.* and *D.m* H3Kc36me3 trimethyllysine analog containing nucleosomes) and increasing
582 PRC2 concentrations (concentrations indicated in the figures above the gels) were performed
583 in triplicates as described in (Choi et al., 2017). A Typhoon FLA 9500 scanner and the Fiji
584 software was used for densitometric analysis of the 6-FAM signal (Schindelin et al., 2012).
585 Background correction and calculation of the fractions of bound nucleosomes was performed
586 with R using tidyverse (https://www.r-project.org/). In detail: two parts were boxed out in each
587 lane: 1. unbound nucleosomes ('unbound' box) and 2. shifted nucleosomes ('bound',
588 everything above 'unbound'). The boxed-out signals were integrated and background corrected
589 by subtracting the respective control ('bound' background of lane 1 for 'bound' boxes and
590 'unbound' background of lane 10 for 'unbound' boxes). To calculate the fraction of bound vs.
591 unbound nucleosomes, the value for 'bound' nucleosome in each lane was divided by the total
592 signal (sum of bound and unbound) of the same lane. Hill function fitting and illustration of
593 the plot were subsequently performed with Prism 8 (GraphPad).
594
595 Histonemethyltransferase (HMTase) assay
596 For all HMTase assays, 446 nM of mononucleosomes or 223 nM of dinucleosomes were
597 incubated with indicated amounts of the different PRC2 complexes, in a reaction buffer
598 containing 20 mM HEPES pH 7.8, 50 mM NaCl, 2.5 mM $MgCl_2$, 5% glycerol, 0.25 mM EDTA,
599 0.5 mM DTT and 80 µM S-adenosylmethionine (SAM). Reactions were allowed to proceed for
600 90 min at RT before quenching by the addition of 1x (final concentration) SDS loading buffer
601 and heat inactivation at 95 °C for 5 min. Proteins were separated by electrophoresis on a 16%
602 (w/v) SDS gel, transferred to a nitrocellulose membrane and probed with antibodies against
603 H3K27me3 (Millipore, 07-449), H3K27me1 (Millipore, 07-448) and H4 (Abcam, ab10158).
604 For quantification, HMTase reactions and the corresponding western blots on *D.m.* unmodified,
605 H3Kc36me3, $H3^{K36A/R}$ mononucleosomes were performed in triplicates and subjected to
606 densitometric analysis (Chemiluminescence signal, ImageQuant LAS 4000). The integrated
607 densitometric signal (band) in each lane was background corrected against the control lane (lane
608 1, no PRC2 in the reaction) and normalized with respect to the lane containing the highest
609 amount (i.e. 100%) of PRC2 on unmodified nucleosomes (lane 4). The relative amounts of
610 trimethylation/monomethylation for all other lanes were calculated with respect to lane 4.
611 Graphical representations were made with Prism 8 (GraphPad).
612
613 Mass Spectrometry (MS)
614 500 nM of PRC2 were incubated with 2 µM of either unmodified or $H3_{18-42}$ peptide containing
615 the K36me3 modification in HMTase reaction buffer (described above) and methyltransferase
616 activity was allowed to proceed over night at RT. Reactions were then quenched with 1%
617 trifluoroacetic acid (TFA). Home-made stage tips with poly(styrenedivinylbenzene) copolymer
618 (SDB-XC) were used to remove PRC2 from the reactions (Rappsilber et al., 2007). First, stage
619 tips were washed with methanol, followed by a second wash with buffer B (0.1% (v/v) formic

620 acid, 80% (v/v) acetonitrile). The SDB-XC material was then equilibrated with buffer A (0.1%
621 (v/v) formic acid) and 40 µl of sample was applied and washed several times. Finally, samples
622 were eluted using buffer B and introduced into the Bruker maXis II ETD mass spectrometer by
623 flow injection of 20 µl sample using an Agilent HPLC at a flow rate of 250 µl/min and 0.05%
624 TFA in 70% acetonitril:H2O as solvent for ESI-MS time-of-flight analysis.
625 Peptides were ionized at a capillary voltage of 4500 V and an end plate offset of 500 V.
626 Full scan MS spectra (200-1600 m/z) were acquired at a spectra rate of 1 Hz and a collision cell
627 energy of 15 eV.
628 Raw data files were processed using Bruker Compass DataAnalysis. The m/z spectra were
629 deconvoluted (maximum entropy method) with an instrument resolving power of 10,000 and
630 the resulting neutral spectra peaks were integrated. For quantification, the experiment was
631 performed in triplicates. The sum of the monomethylation peak areas was divided by the sum
632 of the first 4 peaks of the input peptide together with the sum of the monomethylation peak
633 areas. Illustration of the quantification was subsequently performed with Prism 8 (GraphPad).
634 A Welch's t-test was calculated to show the nonsignificant difference between the activity of
635 PRC2 on unmodified or H3K36me3 peptide.
636
637 Construction of histone transgenes to generate *H3^{K36A}* and *H3^{K36R}* strains
638 Site directed mutagenesis on *pENTR221-HisGU.WT, pENTRL4R1-HisGU.WT* and
639 *pENTRR2L3-HisGU.WT* (Günesdogan et al., 2010) was used to mutate histone H3K36 to
640 alanine or arginine. The final constructs *pfC31-attB-3xHisGU.H3K36A* and *pfC31-attB-*
641 *3xHisGU.H3K36R* were generated by Gateway LR recombination of above vectors and
642 integrated at attP sites VK33 (BDSC 9750) and 86Fb (BDSC 130437). The full genotypes of
643 animals used in the study is described below.
644
645 *Drosophila* strains and genotypes
646 The following strains were used in this study:
647
648 *Oregon-R*
649
650 *w; Df(2L)His^{C} FRT40A/ Df(2L)His^{C} FRT40A; 12xHisGU^{wt}/ 12xHisGU^{wt}* (McKay et al., 2015)
651
652 *w; Df(2L)His^{C} FRT40A/ CyO ubi-GFP; 12xHisGU^{H3K36R}/TM6B* (McKay et al., 2015)
653
654 *w; Df(2L)His^{C} FRT40A/ CyO twi:Gal4 UAS:GFP; 3xHisGU^{H3K36A}(VK33) 3xHisGU^{H3K36A}(86Fb)/ 3xHisGU^{H3K36A}(VK33) 3xHisGU^{H3K36A}(86Fb)*
655 (generated in this study)
656
657 *w; Df(2L)His^{C} FRT40A/ CyO ubi:GFP; 3xHisGU^{H3K27R}(68E) 3xHisGU^{H3K27R} (86Fb)/ 3xHisGU^{H3K27R} (68E) 3xHisGU^{H3K27R} (86Fb)* (Pengelly et al.,
658 2013)
659
660 *w hs-flp; w; hs-nGFP FRT40A/ hs-nGFP FRT40; 3xHisGU^{H3K27R}(68E) 3xHisGU^{H3K27R}(86Fb)/ 3xHisGU^{H3K27R}(68E) 3xHisGU^{H3K27R} (86Fb)* (Pengelly
661 et al., 2013)
662
663 *w hs-flp; M(2)25A ubi-GFP FRT40A/CyO*
664
665 *yw; esc^{6} b pr / CyO, P[esc^{+}]*
666
667 *In(2LR) Gla / CyO, esc^{2}*
668
669
670 The following genotypes were used for the experiments shown in:
671
672 **Figure 4A, C, E**
673 *wt:* *Df(2L) HisC FRT40/ Df(2L) HisC FRT40; 12xHisGU^{wt}(VK33)/ 12xHisGU^{wt}(VK33)*
674 *H3^{K36R}:* *Df(2L) HisC FRT40/ Df(2L) HisC FRT40; 12xHisGU^{H3K36R}(VK33)/TM6B*
675
676 **Figure 4B, D, F**
677 *wt:* *Oregon-R*
678 *H3^{K36A}:* *w; Df(2L)His^{C} FRT40A/ Df(2L)His^{C} FRT40A; 3xHisGU^{H3K36A}(VK33) 3xHisGU^{H3K36A}(86Fb)/ 3xHisGU^{H3K36A}(VK33) 3xHisGU^{H3K36A}(86Fb)*
679
680 **Figure 5A**
681 *wt:* *Df(2L) HisC FRT40/ Df(2L) HisC FRT40; 12xHisGU^{wt}(VK33)/ 12xHisGU^{wt}(VK33)*

682 *$H3^{K36R}$:* *Df(2L) HisC FRT40/ Df(2L) HisC FRT40; 12xHisGU^{H3K36R}(VK33)/TM6B*
683 *$H3^{K36A}$:* *w; Df(2L)His^{C} FRT40A/ Df(2L)His^{C} FRT40A; 3xHisGU^{H3K36A}(VK33) 3xHisGU^{H3K36A}(86Fb)/ 3xHisGU^{H3K36A}(VK33) 3xHisGU^{H3K36A}(86Fb)*
684 *$H3^{K27R}$:* *w; Df(2L)His^{C} FRT40A/ Df(2L)His^{C} FRT40A; 3xHisGU^{H3K27R}(68E) 3xHisGU^{H3K27R} (86Fb)/ 3xHisGU^{H3K27R} (68E) 3xHisGU^{H3K27R} (86Fb)*
685 *esc^{-}:* *esc^{6} b pr / CyO, esc^{2} (esc$^{mat-zyg-}$* obtained as progeny from *esc^{6} b pr/CyO, esc^{2}* parents)
686
687 **Figure 5B**
688 *wt:* *Df(2L) HisC FRT40/ Df(2L) HisC FRT40; 12xHisGU^{wt}(VK33)/ 12xHisGU^{wt}(VK33)*
689 *$H3^{K36R}$:* *Df(2L) HisC FRT40/ Df(2L) HisC FRT40; 12xHisGU^{H3K36R}(VK33)/TM6B*
690
691 **Figure 5C**
692 *wt:* *Df(2L) HisC FRT40/ Df(2L) HisC FRT40; 12xHisGU^{wt}(VK33)/ 12xHisGU^{wt}(VK33)*
693 *$H3^{K36R}$:* *Df(2L) HisC FRT40/ Df(2L) HisC FRT40; 12xHisGU^{H3K36R}(VK33)/TM6B*
694 *$H3^{K27R}$:* *w hs-flp; Df(2L)His^{C} FRT40A/hs-nGFP FRT40A; 3xHisGU^{H3K27R}(68E)3xHisGU^{H3K27R}(86Fb)/3xHisGU^{H3K27R}(68E)3xHisGU^{H3K27R}(86Fb)*
695
696 **Figure 5D**
697 *wt:* *Df(2L) HisC FRT40/ Df(2L) HisC FRT40; 12xHisGU^{wt}(VK33)/ 12xHisGU^{wt}(VK33)*
698 *$H3^{K36R}$:* *Df(2L) HisC FRT40/ Df(2L) HisC FRT40; 12xHisGU^{H3K36R}(VK33)/ TM6B*
699 *$H3^{K36A}$:* *w hs-flp; Df(2L)HisC FRT40A/ M(2)25AubiGFP FRT40; 3xHisGU^{H3K36A}(VK33) 3xHisGU^{H3K36R}(86Fb)/ +*
700 *$H3^{K27R}$:* *w hs-flp; Df(2L)HisC FRT40A/ M(2)25A ubi-GFP FRT40; 3xHisGU^{H3K27R}(68E) 3xHisGU^{H3K27R} (86Fb)/ +*
701
702 **Figure S7**
703 *wt:* *Df(2L) HisC FRT40/ Df(2L) HisC FRT40; 12xHisGU^{wt}(VK33)/ 12xHisGU^{wt}(VK33)*
704 *$H3^{K36R}$:* *Df(2L) HisC FRT40/ Df(2L) HisC FRT40; 12xHisGU^{H3K36R}(VK33)/TM6B*
705 *$H3^{K36A}$:* *Df(2L)His^{C} FRT40A/ Df(2L)His^{C} FRT40A; 3xHisGU^{H3K36A}(VK33) 3xHisGU^{H3K36A}(86Fb)/ 3xHisGU^{H3K36A}(VK33) 3xHisGU^{H3K36A}(86Fb)*
706
707
708 Immunohistochemistry and immunofluorescence stainings
709 Embryos of the appropriate genotypes listed above were identified by the lack of GFP marked
710 balancer chromosomes, fixed and stained with Abd-B antibody, following standard protocols.
711 Imaginal discs from third instar larvae were stained with Antp and Cy3-labeled secondary
712 antibodies following standard protocols. For clonal analysis (**Fig. 3D**), clones were induced 96
713 hrs before analyses by heat-shocked induced expression of Flp recombinase in the genotypes
714 listed above.
715
716 ChIP-seq analysis in *Drosophila* embryos and in larval tissues
717 *Embryo collection, chromatin preparation and ChIP*:_21-24 hr old *wt*, *$H3^{K36A}$* embryos (see
718 above for details of genotypes) were dechorionated, quick-frozen in liquid N2 and stored at -
719 80˚C. 5 µL of thawed embryos were homogenized in 5 mL of fixing solution (60 mM KCl, 15
720 mM NaCl, 4 mM $MgCl_2$, 15 mM Hepes pH 7.6, 0.5% Triton X-100, 0.5 mM DTT, protease
721 inhibitors, 0.9% Formaldehyde) at r.t.. The homogenate was filtered through a strainer (Greiner
722 Bio-One, EASYstrainer^{TM} 100 µm, #542 000) and incubated for 10 min with frequent gentle
723 shaking. Cross-linking was stopped by the addition of 450 µL of 2.5 M Glycine. Fixed nuclei
724 were washed with 1 mL of buffer A1 (60 mM KCl, 15 mM NaCl, 4 mM $MgCl_2$, 15 mM Hepes
725 pH 7.6, 0.5% Triton X-100, 0.5 mM DTT, protease inhibitors), washed with 1 mL of pre-lysis
726 buffer (140 mM NaCl, 15 mM Hepes pH 7.6, 1 mM EDTA, 0.5 mM EGTA, 1% Triton X-100,
727 0.5 mM DTT, 0.1% Na Deoxycholate, protease inhibitors), resuspended in 1 mL of lysis buffer
728 (140 mM NaCl, 15 mM Hepes pH 7.6, 1 mM EDTA, 0.5 mM EGTA, 1% Triton X-100, 0.5
729 mM DTT, 0.1% Na Deoxycholate, protease inhibitors, 0.1% SDS, 0.5% N-laurylsarcosine),
730 incubated at least 10 min at 4˚C with shaking, and transferred into milliTUBES 1 mL AFA
731 Fiber (100) (Covaris, #520130) for sonication. Sonication was performed in a Covaris S220
732 AFA instrument using the following setup: 140W (peak incident power) / 5% (duty cycle) / 200
733 (cycle per burst) / 15 min. Insoluble material was removed by centrifugation in an Eppendorf
734 centrifuge at 14000 rpm (10 min at 4°C). Input chromatin was quantified by measuring DNA
735 concentration after decrosslinking using Qubit (Thermo Scientific) and 250 ng of chromatin
736 were used for each ChIP experiment. 250 ng of an independently prepared batch of *D.*
737 *pseudoobscura* chromatin were spiked-in in each ChIP experiment for subsequent
738 normalization of the ChIP-seq datasets. The rest of the ChIP protocol was performed as
739 described (Bonnet et al., 2019). For each condition, the ChIP experiment was performed in
740 duplicates from two biologically independent chromatins. ChIP on hand-dissected CNS and
741 imaginal disc tissues from 3rd instar *wt* or *$H3^{K36R}$* homozygous larvae (see above for details on

742 genotypes) was performed as described (Laprell et al., 2017) with the difference *D.*
743 *pseudoobscura* chromatin was spiked in at a 1:1 ratio of dm / dp chromatin.
744 *Library preparation and sequencing*: Library preparation for sequencing was performed with
745 TruSeq kits from Illumina. Illumina systems (NextSeq 500) were used for paired-end DNA
746 sequencing. All reads were aligned using STAR (Dobin et al., 2013) to the *D. melanogaster*
747 dm6 genome assembly (Santos et al., 2015) and to the *D. pseudoobscura* dp3 genome assembly
748 (Nov. 2004, FlyBase Release 1.03). Only sequences that mapped uniquely to the genome with
749 a maximum of two mismatches were considered for further analyses.
750 *Identification of H3K36me2 and H3K27me3 enriched regions*: The Bioconductor STAN-
751 package (Zacher et al., 2017) was used to define the location of H3K36me2-enriched regions.
752 The seven chromosome arms (X, 2L, 2R, 3L, 3R, 4 and Y) defined in the dm6 genome assembly
753 were segmented in 200 bp bins. STAN annotated each of these bins into 1 of 3 'genomic states'
754 based on the number of H3K36me2 ChIP-seq reads and the number of input reads overlapping
755 with each bin, in 21-24 hr wild-type embryos. These 3 'genomic states' corresponded to:
756 'H3K36me2 enriched' regions; 'low or no H3K36me2' regions and 'no input' regions. The
757 Poisson Lognormal distribution was selected and fitting of hidden Markov models was
758 performed with a maximum number of 100 iterations. Stretches of consecutive bins annotated
759 as 'H3K36me2 enriched' regions were sometimes separated by a few bins showing another
760 type of annotation (i.e. 'no input'). To define a relevant set of H3K36me2 enriched regions, we
761 considered that if stretches of consecutive bins annotated as 'H3K36me2 enriched' regions are
762 not separated by more than 7 Kb, they can be fused. High-level H3K27me3 domains previously
763 defined using the same Bioconductor STAN-package in Bonnet et al (Bonnet et al., 2019) were
764 used in this study.
765 *Normalization and visualisation of H3K27me3 and H3K36me2 ChIP-Seq datasets*: The
766 proportion of *D. pseudoobscura* reads as compared to *D. melanogaster* reads in input and in
767 samples was used to normalize the H3K36me2 and H3K27me3 ChIP-seq datasets from $H3^{K36A}$
768 and $H3^{K36R}$ mutants to the corresponding wild-type H3K36me2 and H3K27me3 ChIP-seq
769 datasets respectively (see Table S2). Chip-seq tracks shown in Fig. 4 show the average of the
770 two biological replicates that were performed for each condition. Y-axes of ChIP-seq tracks
771 correspond to normalized numbers of mapped reads per million reads per 200 bp bin.
772 *Calculation of read coverage*: In wild-type and $H3^{K36A\ and\ R}$ mutant conditions, H3K36me2 and
773 H3K27me3 ChIP-seq read coverages across gene bodies were computed on genomic intervals
774 starting 750 bp upstream transcription start sites and ending 750 bp downstream transcription
775 termination sites. Read coverage is defined as the normalized number of mapped reads per
776 million reads from a ChIP-seq dataset divided by the number of mapped reads per million reads
777 from the corresponding input dataset across a genomic region. Among the *D. melanogaster*
778 Refseq genes, approximately 10800 and 9200 are overlapping with H3K36me2 enriched
779 regions, approximately 1030 and 1030 genes are overlapping with high-level H3K27me3
780 domains and 5400 and 6300 are localized in other genomic regions in embryos and larvae,
781 respectively.
782
783 <u>*Drosophila* nuclear and cell extracts for western blot analysis</u>
784 For embryonic total nuclear extracts, nuclei from 21-24 hr old *wt*, $H3^{K36A}$ or $H3^{K36A}$ mutant
785 embryos were purified and quantified as described (Bonnet et al., 2019). Pellets of nuclei were
786 resuspended in appropriate volumes of SDS sample buffer proportional to the number of nuclei
787 in each pellet. Extracts were then sonicated in a Bioruptor instrument (Diagenode) (8 cycles
788 (30 sec ON / 30 sec OFF), high power mode), incubated at 75˚C for 5 min and insoluble material
789 was removed by centrifugation at 14000 rpm for 1 mn at r.t..
790 Total cell extracts from imaginal disc tissues were prepared by resuspending hand-dissected
791 disc tissues in SDS sample buffer. Extracts were then sonicated, incubated at 75˚C for 5 min
792 and insoluble material was removed by centrifugation.
793
794 <u>Antibodies</u>
795 For ChIP analysis:
796 Rabbit monoclonal anti-H3K27me3 Cell Signaling Technology #9733

Rabbit polyclonal anti-H3K36me2	Abcam	#9049

For Western blot analysis on embryonic and larval extracts:

Rabbit monoclonal anti-H3K27me3	Cell Signaling Technology	#9733
Rabbit polyclonal anti- H3K27me3	Millipore	#07-449
Rabbit polyclonal anti-H3K27me1	Millipore	#07-448
Rabbit monoclonal anti-H3K36me3	Cell Signaling Technology	#4909
Rabbit monoclonal anti-H3K36me2	Cell Signaling Technology	#2901
Rabbit polyclonal anti-H2B	(against full-length recombinant D.m. H2B)	
Rabbit polyclonal anti-H4	Abcam	#10158
Rabbit polyclonal anti-Caf1	(Gambetta et al., 2009)	

For immunohistochemistry and immunofluorescence analysis:

Mouse monoclonal anti-Abd-B	DSHB (1A2E9)
Mouse monoclonal anti-Antp	DSHB (8C11)

ACKNOWLEDGMENTS

We thank Eva Nogales for generous advice, sharing of expertise and for hosting K.F. for grid preparation. We thank Tom Cech for stimulating discussions. We thank J.R. Prabu for excellent computing support, S.Uebel, E.Weyher, R.Kim and A.Yeroslaviz of the MPIB core facilities for excellent technical support and S.Schkoelziger and S.Schmähling for help with some of the experiments. This work was supported by the Deutsche Forschungsgemeinschaft (SFB1064) and the MPG. ChIP-seq data have been deposited in GEO (accession number: GSE148254).

823 **REFERENCES**

824

825 Afonine, P.V., Poon, B.K., Read, R.J., Sobolev, O.V., Terwilliger, T.C., Urzhumtsev, A.,
826 Adams, P.D., 2018. Real-space refinement in PHENIX for cryo-EM and crystallography.
827 Acta Crystallogr D Struct Biol 74, 531–544. doi:10.1107/S2059798318006551
828 Bai, X.-C., Rajendra, E., Yang, G., Shi, Y., Scheres, S.H.W., 2015. Sampling the
829 conformational space of the catalytic subunit of human γ-secretase. Elife 4, 1485.
830 doi:10.7554/eLife.11182
831 Ballaré, C., Lange, M., Lapinaite, A., Martin, G.M., Morey, L., Pascual, G., Liefke, R.,
832 Simon, B., Shi, Y., Gozani, O., Carlomagno, T., Benitah, S.A., Di Croce, L., 2012. Phf19
833 links methylated Lys36 of histone H3 to regulation of Polycomb activity. Nat. Struct.
834 Mol. Biol. 19, 1257–1265. doi:10.1038/nsmb.2434
835 Bonnet, J., Lindeboom, R.G.H., Pokrovsky, D., Stricker, G., Çelik, M.H., Rupp, R.A.W.,
836 Gagneur, J., Vermeulen, M., Imhof, A., Müller, J., 2019. Quantification of Proteins and
837 Histone Marks in Drosophila Embryos Reveals Stoichiometric Relationships Impacting
838 Chromatin Regulation. Dev. Cell 51, 632–644.e6. doi:10.1016/j.devcel.2019.09.011
839 Cai, L., Rothbart, S.B., Lu, R., Xu, B., Chen, W.-Y., Tripathy, A., Rockowitz, S., Zheng, D.,
840 Patel, D.J., Allis, C.D., Strahl, B.D., Song, J., Wang, G.G., 2013. An H3K36
841 methylation-engaging Tudor motif of polycomb-like proteins mediates PRC2 complex
842 targeting. Mol. Cell 49, 571–582. doi:10.1016/j.molcel.2012.11.026
843 Casañal, A., Lohkamp, B., Emsley, P., 2020. Current developments in Coot for
844 macromolecular model building of Electron Cryo-microscopy and Crystallographic Data.
845 Protein Sci. 29, 1069–1078. doi:10.1002/pro.3791
846 Chen, S., Jiao, L., Liu, X., Yang, X., Liu, X., 2020. A Dimeric Structural Scaffold for PRC2-
847 PCL Targeting to CpG Island Chromatin. Mol. Cell 77, 1265–1278.e7.
848 doi:10.1016/j.molcel.2019.12.019
849 Chen, S., Jiao, L., Shubbar, M., Yang, X., Liu, X., 2018. Unique Structural Platforms of
850 Suz12 Dictate Distinct Classes of PRC2 for Chromatin Binding. Mol. Cell 69, 840–
851 852.e5. doi:10.1016/j.molcel.2018.01.039
852 Choi, J., Bachmann, A.L., Tauscher, K., Benda, C., Fierz, B., Müller, J., 2017. DNA binding
853 by PHF1 prolongs PRC2 residence time on chromatin and thereby promotes H3K27
854 methylation. Nat. Struct. Mol. Biol. 298, 1039. doi:10.1038/nsmb.3488
855 Copur, Ö., Gorchakov, A., Finkl, K., Kuroda, M.I., Müller, J., 2018. Sex-specific phenotypes
856 of histone H4 point mutants establish dosage compensation as the critical function of
857 H4K16 acetylation in Drosophila. Proc Natl Acad Sci USA 115, 13336–13341.
858 doi:10.1073/pnas.1817274115
859 Dobin, A., Davis, C.A., Schlesinger, F., Drenkow, J., Zaleski, C., Jha, S., Batut, P., Chaisson,
860 M., Gingeras, T.R., 2013. STAR: ultrafast universal RNA-seq aligner. Bioinformatics 29,
861 15–21. doi:10.1093/bioinformatics/bts635
862 Dorafshan, E., Kahn, T.G., Glotov, A., Savitsky, M., Walther, M., Reuter, G., Schwartz, Y.B.,
863 2019. Ash1 counteracts Polycomb repression independent of histone H3 lysine 36
864 methylation. EMBO Rep. e46762. doi:10.15252/embr.201846762
865 Emsley, P., Lohkamp, B., Scott, W.G., Cowtan, K., 2010. Features and development of Coot.
866 Acta Crystallogr. D Biol. Crystallogr. 66, 486–501. doi:10.1107/S0907444910007493
867 Francis, N.J., Kingston, R.E., Woodcock, C.L., 2004. Chromatin compaction by a polycomb
868 group protein complex. Science 306, 1574–1577. doi:10.1126/science.1100576
869 Gambetta, M.C., Oktaba, K., Müller, J., 2009. Essential role of the glycosyltransferase
870 sxc/Ogt in polycomb repression. Science 325, 93–96. doi:10.1126/science.1169727
871 Gaydos, L.J., Rechtsteiner, A., Egelhofer, T.A., Carroll, C.R., Strome, S., 2012. Antagonism
872 between MES-4 and Polycomb repressive complex 2 promotes appropriate gene
873 expression in C. elegans germ cells. Cell Rep 2, 1169–1177.
874 doi:10.1016/j.celrep.2012.09.019

875 Goddard, T.D., Huang, C.C., Meng, E.C., Pettersen, E.F., Couch, G.S., Morris, J.H., Ferrin,
876 T.E., 2018. UCSF ChimeraX: Meeting modern challenges in visualization and analysis.
877 Protein Sci. 27, 14–25. doi:10.1002/pro.3235
878 Grau, D.J., Chapman, B.A., Garlick, J.D., Borowsky, M., Francis, N.J., Kingston, R.E., 2011.
879 Compaction of chromatin by diverse Polycomb group proteins requires localized regions
880 of high charge. Genes Dev. 25, 2210–2221. doi:10.1101/gad.17288211
881 Guidotti, N., Lechner, C.C., Bachmann, A.L., Fierz, B., 2019. A Modular Ligation Strategy
882 for Asymmetric Bivalent Nucleosomes Trimethylated at K36 and K27. Chembiochem
883 20, 1124–1128. doi:10.1002/cbic.201800744
884 Günesdogan, U., Jäckle, H., Herzig, A., 2010. A genetic system to assess in vivo the functions
885 of histones and histone modifications in higher eukaryotes. EMBO Rep. 11, 772–776.
886 doi:10.1038/embor.2010.124
887 Hansen, K.H., Bracken, A.P., Pasini, D., Dietrich, N., Gehani, S.S., Monrad, A., Rappsilber,
888 J., Lerdrup, M., Helin, K., 2008. A model for transmission of the H3K27me3 epigenetic
889 mark. Nat. Cell Biol. 10, 1291–1300. doi:10.1038/ncb1787
890 Henderson, R., Sali, A., Baker, M.L., Carragher, B., Devkota, B., Downing, K.H., Egelman,
891 E.H., Feng, Z., Frank, J., Grigorieff, N., Jiang, W., Ludtke, S.J., Medalia, O., Penczek,
892 P.A., Rosenthal, P.B., Rossmann, M.G., Schmid, M.F., Schröder, G.F., Steven, A.C.,
893 Stokes, D.L., Westbrook, J.D., Wriggers, W., Yang, H., Young, J., Berman, H.M., Chiu,
894 W., Kleywegt, G.J., Lawson, C.L., 2012. Outcome of the first electron microscopy
895 validation task force meeting., in:. Presented at the Structure (London, England : 1993),
896 pp. 205–214. doi:10.1016/j.str.2011.12.014
897 Ilca, S.L., Kotecha, A., Sun, X., Poranen, M.M., Stuart, D.I., Huiskonen, J.T., 2015.
898 Localized reconstruction of subunits from electron cryomicroscopy images of
899 macromolecular complexes. Nat Commun 6, 8843–8. doi:10.1038/ncomms9843
900 Jani, K.S., Jain, S.U., Ge, E.J., Diehl, K.L., Lundgren, S.M., Müller, M.M., Lewis, P.W.,
901 Muir, T.W., 2019. Histone H3 tail binds a unique sensing pocket in EZH2 to activate the
902 PRC2 methyltransferase. Proc. Natl. Acad. Sci. U.S.A. 116, 8295–8300.
903 doi:10.1073/pnas.1819029116
904 Jiao, L., Liu, X., 2015. Structural basis of histone H3K27 trimethylation by an active
905 polycomb repressive complex 2. Science 350, aac4383–aac4383.
906 doi:10.1126/science.aac4383
907 Justin, N., Zhang, Y., Tarricone, C., Martin, S.R., Chen, S., Underwood, E., De Marco, V.,
908 Haire, L.F., Walker, P.A., Reinberg, D., Wilson, J.R., Gamblin, S.J., 2016. Structural
909 basis of oncogenic histone H3K27M inhibition of human polycomb repressive complex
910 2. Nat Commun 7, 11316. doi:10.1038/ncomms11316
911 Kasinath, V., Beck, C., Sauer, P., Poepsel, S., Kosmatka, J., Faini, M., Toso, D., Aebersold,
912 R., Nogales, E., 2020. JARID2 and AEBP2 regulate PRC2 activity in the presence of
913 H2A ubiquitination or other histone modifications. bioRxiv 2020.04.20.049213.
914 Kasinath, V., Faini, M., Poepsel, S., Reif, D., Feng, X.A., Stjepanovic, G., Aebersold, R.,
915 Nogales, E., 2018. Structures of human PRC2 with its cofactors AEBP2 and JARID2.
916 Science 359, 940–944. doi:10.1126/science.aar5700
917 Klymenko, T., Müller, J., 2004. The histone methyltransferases Trithorax and Ash1 prevent
918 transcriptional silencing by Polycomb group proteins. EMBO Rep. 5, 373–377.
919 doi:10.1038/sj.embor.7400111
920 Laprell, F., Finkl, K., Müller, J., 2017. Propagation of Polycomb-repressed chromatin requires
921 sequence-specific recruitment to DNA. Science 356, 85–88. doi:10.1126/science.aai8266
922 Laugesen, A., Højfeldt, J.W., Helin, K., 2019. Molecular Mechanisms Directing PRC2
923 Recruitment and H3K27 Methylation. Mol. Cell 74, 8–18.
924 doi:10.1016/j.molcel.2019.03.011
925 Li, H., Liefke, R., Jiang, J., Kurland, J.V., Tian, W., Deng, P., Zhang, W., He, Q., Patel, D.J.,
926 Bulyk, M.L., Shi, Y., Wang, Z., 2017. Polycomb-like proteins link the PRC2 complex to
927 CpG islands. Nature. doi:10.1038/nature23881

928 Lowary, P.T., Widom, J., 1998. New DNA sequence rules for high affinity binding to histone
929 octamer and sequence-directed nucleosome positioning. J. Mol. Biol. 276, 19–42.
930 doi:10.1006/jmbi.1997.1494
931 Luger, K., Mäder, A.W., Richmond, R.K., Sargent, D.F., Richmond, T.J., 1997. Crystal
932 structure of the nucleosome core particle at 2.8 A resolution. Nature 389, 251–260.
933 doi:10.1038/38444
934 Luger, K., Rechsteiner, T.J., Richmond, T.J., 1999. Preparation of nucleosome core particle
935 from recombinant histones. Meth. Enzymol. 304, 3–19.
936 Margueron, R., Justin, N., Ohno, K., Sharpe, M.L., Son, J., Drury, W.J., Voigt, P., Martin,
937 S.R., Taylor, W.R., De Marco, V., Pirrotta, V., Reinberg, D., Gamblin, S.J., 2009. Role
938 of the polycomb protein EED in the propagation of repressive histone marks. Nature 461,
939 762–767. doi:10.1038/nature08398
940 McGinty, R.K., Henrici, R.C., Tan, S., 2014. Crystal structure of the PRC1 ubiquitylation
941 module bound to the nucleosome. Nature 514, 591–596. doi:10.1038/nature13890
942 McKay, D.J., Klusza, S., Penke, T.J.R., Meers, M.P., Curry, K.P., McDaniel, S.L., Malek,
943 P.Y., Cooper, S.W., Tatomer, D.C., Lieb, J.D., Strahl, B.D., Duronio, R.J., Matera, A.G.,
944 2015. Interrogating the function of metazoan histones using engineered gene clusters.
945 Dev. Cell 32, 373–386. doi:10.1016/j.devcel.2014.12.025
946 Meers, M.P., Henriques, T., Lavender, C.A., McKay, D.J., Strahl, B.D., Duronio, R.J.,
947 Adelman, K., Matera, A.G., 2017. Histone gene replacement reveals a post-
948 transcriptional role for H3K36 in maintaining metazoan transcriptome fidelity. Elife 6,
949 1191. doi:10.7554/eLife.23249
950 Musselman, C.A., Gibson, M.D., Hartwick, E.W., North, J.A., Gatchalian, J., Poirier, M.G.,
951 Kutateladze, T.G., 2013. Binding of PHF1 Tudor to H3K36me3 enhances nucleosome
952 accessibility. Nat Commun 4, 2969–9. doi:10.1038/ncomms3969
953 Nekrasov, M., Wild, B., Müller, J., 2005. Nucleosome binding and histone methyltransferase
954 activity of Drosophila PRC2. EMBO Rep. 6, 348–353. doi:10.1038/sj.embor.7400376
955 Pengelly, A.R., Copur, Ö., Jäckle, H., Herzig, A., Müller, J., 2013. A histone mutant
956 reproduces the phenotype caused by loss of histone-modifying factor Polycomb. Science
957 339, 698–699. doi:10.1126/science.1231382
958 Pettersen, E.F., Goddard, T.D., Huang, C.C., Couch, G.S., Greenblatt, D.M., Meng, E.C.,
959 Ferrin, T.E., 2004. UCSF Chimera--a visualization system for exploratory research and
960 analysis. J Comput Chem 25, 1605–1612. doi:10.1002/jcc.20084
961 Poepsel, S., Kasinath, V., Nogales, E., 2018. Cryo-EM structures of PRC2 simultaneously
962 engaged with two functionally distinct nucleosomes. Nat. Struct. Mol. Biol. 25, 154–162.
963 doi:10.1038/s41594-018-0023-y
964 Rappsilber, J., Mann, M., Ishihama, Y., 2007. Protocol for micro-purification, enrichment,
965 pre-fractionation and storage of peptides for proteomics using StageTips. Nat Protoc 2,
966 1896–1906. doi:10.1038/nprot.2007.261
967 Rosenthal, P.B., Henderson, R., 2003. Optimal determination of particle orientation, absolute
968 hand, and contrast loss in single-particle electron cryomicroscopy. J. Mol. Biol. 333,
969 721–745. doi:10.1016/j.jmb.2003.07.013
970 Rosenthal, P.B., Rubinstein, J.L., 2015. Validating maps from single particle electron
971 cryomicroscopy. Curr. Opin. Struct. Biol. 34, 135–144. doi:10.1016/j.sbi.2015.07.002
972 Santos, dos, G., Schroeder, A.J., Goodman, J.L., Strelets, V.B., Crosby, M.A., Thurmond, J.,
973 Emmert, D.B., Gelbart, W.M., FlyBase Consortium, 2015. FlyBase: introduction of the
974 Drosophila melanogaster Release 6 reference genome assembly and large-scale migration
975 of genome annotations. Nucleic Acids Res. 43, D690–7. doi:10.1093/nar/gku1099
976 Schindelin, J., Arganda-Carreras, I., Frise, E., Kaynig, V., Longair, M., Pietzsch, T.,
977 Preibisch, S., Rueden, C., Saalfeld, S., Schmid, B., Tinevez, J.-Y., White, D.J.,
978 Hartenstein, V., Eliceiri, K., Tomancak, P., Cardona, A., 2012. Fiji: an open-source
979 platform for biological-image analysis. Nat. Methods 9, 676–682.
980 doi:10.1038/nmeth.2019
981 Schmitges, F.W., Prusty, A.B., Faty, M., Stützer, A., Lingaraju, G.M., Aiwazian, J., Sack, R.,
982 Hess, D., Li, L., Zhou, S., Bunker, R.D., Wirth, U., Bouwmeester, T., Bauer, A., Ly-

983 Hartig, N., Zhao, K., Chan, H., Gu, J., Gut, H., Fischle, W., Müller, J., Thomä, N.H.,
984 2011. Histone methylation by PRC2 is inhibited by active chromatin marks. Mol. Cell
985 42, 330–341. doi:10.1016/j.molcel.2011.03.025
986 Simon, M.D., Chu, F., Racki, L.R., la Cruz, de, C.C., Burlingame, A.L., Panning, B.,
987 Narlikar, G.J., Shokat, K.M., 2007. The site-specific installation of methyl-lysine analogs
988 into recombinant histones. Cell 128, 1003–1012. doi:10.1016/j.cell.2006.12.041
989 Sobolev, O.V., Afonine, P.V., Adams, P.D., Urzhumtsev, A., 2015. Programming new
990 geometry restraints: parallelity of atomic groups. J Appl Crystallogr 48, 1130–1141.
991 doi:10.1107/S1600576715010432
992 Streubel, G., Watson, A., Jammula, S.G., Scelfo, A., Fitzpatrick, D.J., Oliviero, G., McCole,
993 R., Conway, E., Glancy, E., Negri, G.L., Dillon, E., Wynne, K., Pasini, D., Krogan, N.J.,
994 Bracken, A.P., Cagney, G., 2018. The H3K36me2 Methyltransferase Nsd1 Demarcates
995 PRC2-Mediated H3K27me2 and H3K27me3 Domains in Embryonic Stem Cells. Mol.
996 Cell 70, 371–379.e5. doi:10.1016/j.molcel.2018.02.027
997 Tan, Y.Z., Baldwin, P.R., Davis, J.H., Williamson, J.R., Potter, C.S., Carragher, B., Lyumkis,
998 D., 2017. Addressing preferred specimen orientation in single-particle cryo-EM through
999 tilting. Nat. Methods 14, 793–796. doi:10.1038/nmeth.4347
1000 Terwilliger, T.C., Ludtke, S.J., Read, R.J., Adams, P.D., Afonine, P.V., 2019. Improvement
1001 of cryo-EM maps by density modification 58, 214–31. doi:10.1101/845032
1002 Wang, X., Paucek, R.D., Gooding, A.R., Brown, Z.Z., Ge, E.J., Muir, T.W., Cech, T.R.,
1003 2017. Molecular analysis of PRC2 recruitment to DNA in chromatin and its inhibition by
1004 RNA. Nat. Struct. Mol. Biol. 24, 1028–1038. doi:10.1038/nsmb.3487
1005 Worden, E.J., Hoffmann, N.A., Hicks, C.W., Wolberger, C., 2019. Mechanism of Cross-talk
1006 between H2B Ubiquitination and H3 Methylation by Dot1L. Cell 176, 1490–1501.e12.
1007 doi:10.1016/j.cell.2019.02.002
1008 Yu, J.-R., Lee, C.-H., Oksuz, O., Stafford, J.M., Reinberg, D., 2019. PRC2 is high
1009 maintenance. Genes Dev. 33, 903–935. doi:10.1101/gad.325050.119
1010 Yuan, W., Xu, M., Huang, C., Liu, N., Chen, S., Zhu, B., 2011. H3K36 methylation
1011 antagonizes PRC2-mediated H3K27 methylation. J. Biol. Chem. 286, 7983–7989.
1012 doi:10.1074/jbc.M110.194027
1013 Zacher, B., Michel, M., Schwalb, B., Cramer, P., Tresch, A., Gagneur, J., 2017. Accurate
1014 Promoter and Enhancer Identification in 127 ENCODE and Roadmap Epigenomics Cell
1015 Types and Tissues by GenoSTAN. PLoS ONE 12, e0169249.
1016 doi:10.1371/journal.pone.0169249
1017 Zhang, K., 2016. Gctf: Real-time CTF determination and correction. J. Struct. Biol. 193, 1–
1018 12. doi:10.1016/j.jsb.2015.11.003
1019 Zheng, S.Q., Palovcak, E., Armache, J.-P., Verba, K.A., Cheng, Y., Agard, D.A., 2017.
1020 MotionCor2: anisotropic correction of beam-induced motion for improved cryo-electron
1021 microscopy. Nat. Methods 14, 331–332. doi:10.1038/nmeth.4193
1022 Zhou, Q., Huang, X., Sun, S., Li, X., Wang, H.-W., Sui, S.-F., 2015. Cryo-EM structure of
1023 SNAP-SNARE assembly in 20S particle. Cell Res. 25, 551–560. doi:10.1038/cr.2015.47
1024 Zivanov, J., Nakane, T., Forsberg, B.O., Kimanius, D., Hagen, W.J., Lindahl, E., Scheres,
1025 S.H., 2018. New tools for automated high-resolution cryo-EM structure determination in
1026 RELION-3. Elife 7, 163. doi:10.7554/eLife.42166
1027
1028

1029

Figure 1

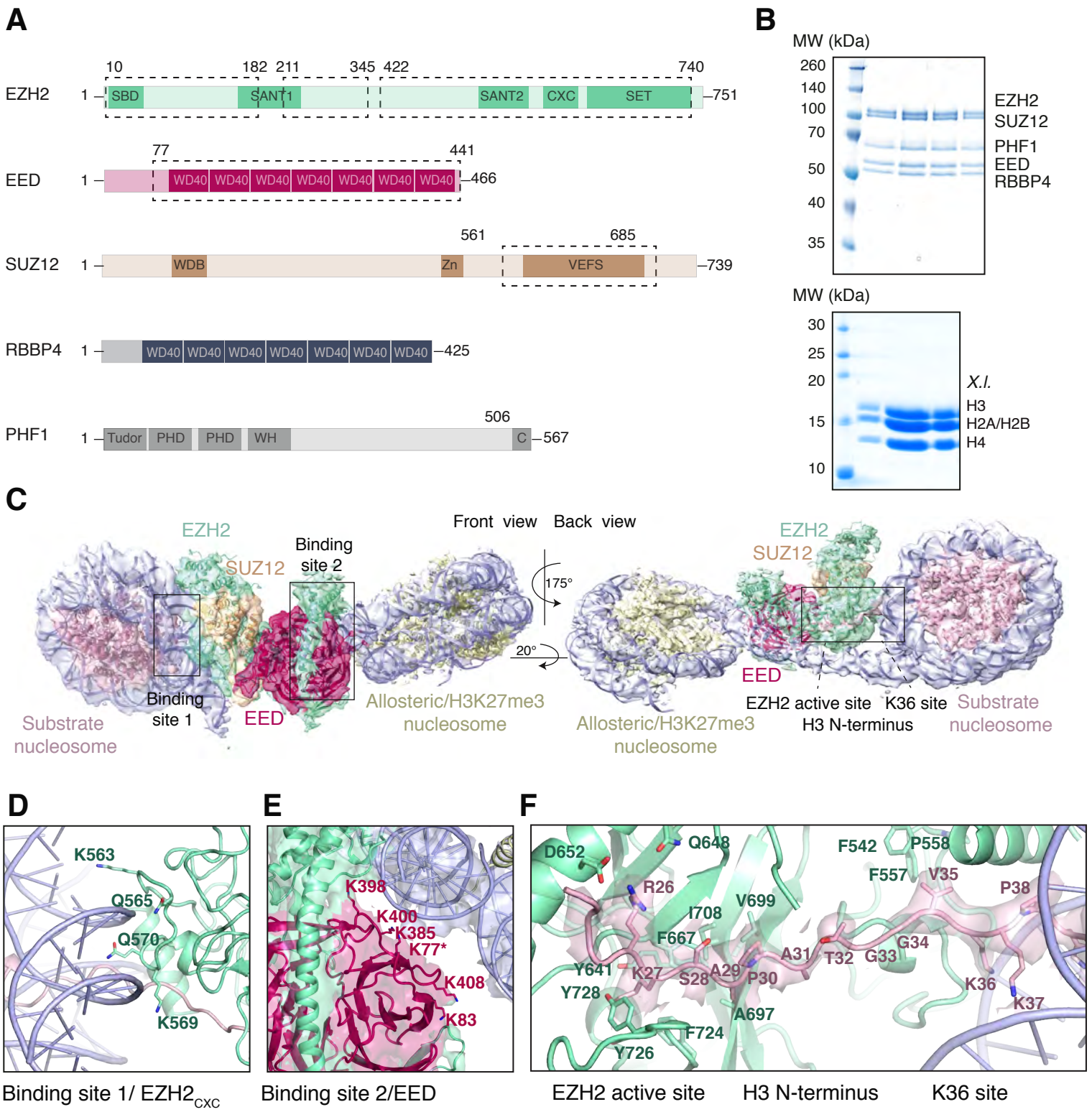
A
EZH2
1
10
182
211
345
422
740
751
SBD
SANT1
SANT2
CXC
SET
EED
77
441
466
WD40
SUZ12
561
685
739
WDB
Zn
VEFS
RBBP4
425
PHF1
506
567
Tudor
PHD
WH
C
B
MW (kDa)
260
140
100
70
50
40
35
EZH2
SUZ12
PHF1
EED
RBBP4
30
25
20
15
10
X.l.
H3
H2A/H2B
H4
C
Front view
Back view
175°
20°
Binding site 2
Binding site 1
Substrate nucleosome
Allosteric/H3K27me3 nucleosome
EZH2 active site
K36 site
H3 N-terminus
D
K563
Q565
Q570
K569
E
K398
K400
*K385
K77*
K408
K83
F
D652
Q648
R26
I708
V699
F667
Y641
K27
S28
A29
P30
A31
T32
G33
G34
F542
P558
F557
V35
P38
K36
K37
Y728
A697
F724
Y726
Binding site 1/ EZH2CXC
Binding site 2/EED
EZH2 active site
H3 N-terminus
K36 site

1030 **FIGURE 1**

1031 **Interaction of the PRC2 catalytic lobe with nucleosomal DNA orients the H3 N-terminus**
1032 **for H3K27 binding to the active site.**

1033 (**A**) Domain organization in the five subunits of PHF1-PRC2. Dashed boxes indicate protein
1034 portions visible in the PHF1-PRC2:di-Nuc cryo-EM reconstruction and fitted in the structural
1035 model. In PHF1, C corresponds to the short C-terminal fragment used in $PHF1_C$-PRC2.

1036 (**B**) Coomassie-stained SDS PAGE analysis of representative PHF1-PRC2 (upper panel)
1037 and *X.l.* octamer preparations (lower panel) after size-exclusion chromatography (SEC)
1038 purification. Pooled fractions of PHF1-PRC2, incubated with heterodimeric dinucleosomes
1039 generated by DNA ligation of a reconstituted unmodified and a H3Kc27me3-modified
1040 mononucleosome were used as input material for cryo-EM analysis.

1041 (**C**) Cryo-EM reconstruction of PHF1-PRC2:di-Nuc in two orientations with fitted crystal
1042 structures of human PRC2 catalytic lobe (PDB: 5HYN, (Justin et al., 2016)) and nucleosomes
1043 (1AOI, (Luger et al., 1997)) in a di-Nuc model with 35 bp linker DNA (see also
1044 **Supplementary Figures 1-4, Table S1, Movie S1**). Density is colored as in (**A**) to show PRC2
1045 subunits, DNA (blue) and octamers of substrate (pink) and allosteric (yellow) nucleosomes.
1046 Boxes indicate regions shown in (**D**), (**E**) and (**F**), respectively.

1047 (**D**) Interaction of $EZH2_{CXC}$ residues with the DNA gyres of the substrate nucleosome; residues
1048 mutated in $PRC2^{CXC>A}$ are indicated. For the H3 N-terminus (pink), only the peptide backbone
1049 is shown in this view (see **F**).

1050 (**E**) Interface formed by EED and the EZH2 SBD domain with DNA gyres on the allosteric
1051 nucleosome; residues mutated in $PRC2^{EED>A}$ are indicated. Asterisk indicates the approximate
1052 location of a residue, which is not built in the model.

1053 (**F**) The H3 N-terminus (pink), shown as a pseudoatomic model fitted into the 4.4 Å density
1054 map, is recognized by EZH2 through an extensive interaction network (see text). Note the well-
1055 defined side-chain density of H3K36 (see also **Supplementary Figure 3D and 4C-E**).

1056

1057

Figure 2

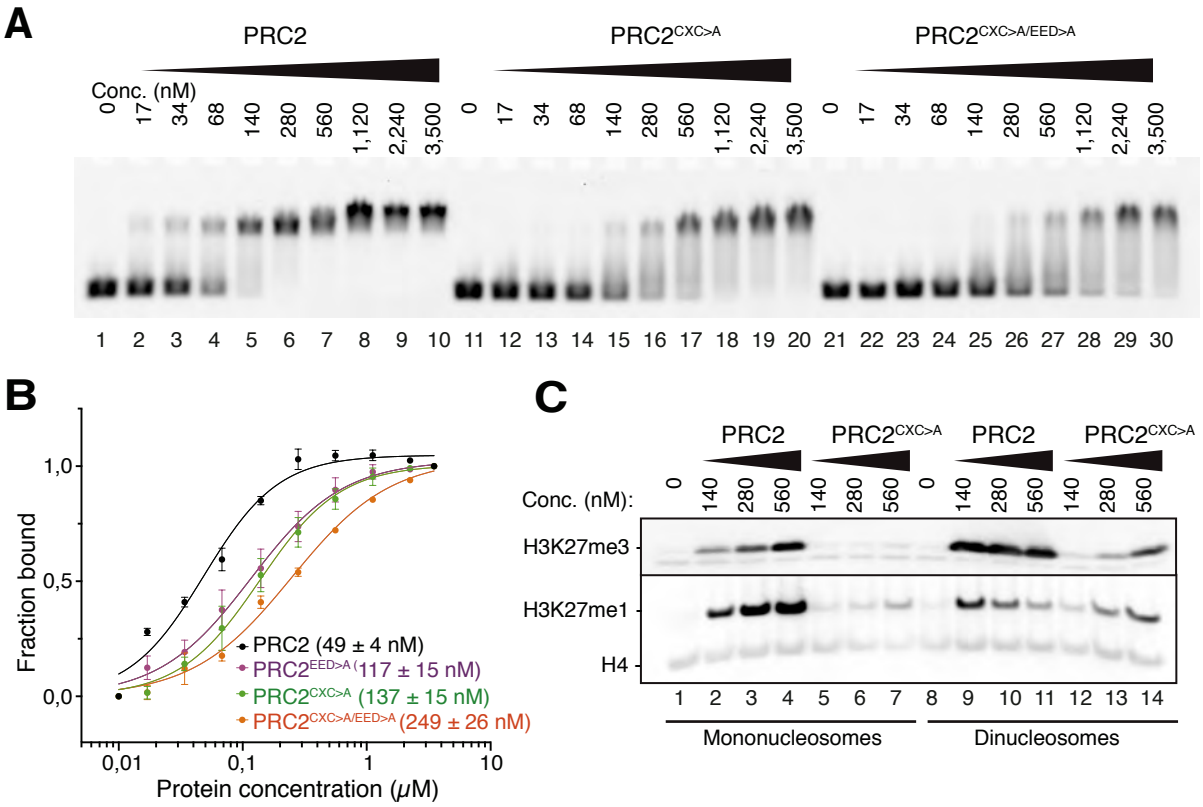
A
PRC2
PRC2CXC>A
PRC2CXC>A/EED>A
Conc. (nM)
0 17 34 68 140 280 560 1,120 2,240 3,500
1 2 3 4 5 6 7 8 9 10 11 12 13 14 15 16 17 18 19 20 21 22 23 24 25 26 27 28 29 30
B
Fraction bound
1,0
0,5
0,0
0,01
0,1
1
10
Protein concentration (μM)
PRC2 (49 ± 4 nM)
PRC2EED>A (117 ± 15 nM)
PRC2CXC>A (137 ± 15 nM)
PRC2CXC>A/EED>A (249 ± 26 nM)
C
PRC2
PRC2CXC>A
PRC2
PRC2CXC>A
Conc. (nM):
0 140 280 560 140 280 560 0 140 280 560 140 280 560
H3K27me3
H3K27me1
H4
1 2 3 4 5 6 7 8 9 10 11 12 13 14
Mononucleosomes
Dinucleosomes

1058 **FIGURE 2**

1059 **The $EZH2_{CXC}$-DNA interaction interface is critical for H3K27 methylation on**
1060 **nucleosomes.**

1061 (**A**) Binding reactions with indicated concentrations of PRC2 (lanes 1-10), $PRC2^{CXC>A}$ (lanes
1062 11-20) or $PRC2^{CXC>A/EED>A}$ (lanes 21-30) and 45 nM 6-carboxyfluorescein-labeled
1063 mononucleosomes, analyzed by EMSA on 1.2% agarose gels; for analysis of $PRC2^{EED>A}$
1064 binding, see **Supplementary Figure 5A**.

1065 (**B**) Quantitative analysis of EMSA data in A by densitometry of 6-carboxyfluorescein signals
1066 from independent experiments (n=3); error bars, SEM.

1067 (**C**) Western Blot (WB) analysis of H3K27me1 and H3K27me3 formation in HMTase reactions
1068 with indicated concentrations of PRC2 and $PRC2^{CXC>A}$ on 446 nM mononucleosomes (lanes 1-
1069 7) or 223 nM dinucleosomes (lanes 8-14). Note that these concentrations result in equal
1070 numbers of nucleosomes and therefore equal numbers of H3 substrate molecules in the
1071 reactions on mono- and dinucleosomes, as can be seen from the Coomassie-stained gel of the
1072 reactions in **Supplementary Figure 5B**. H4 WB signal served as control for Western blot
1073 processing.

1074

1075

1076

Figure 3

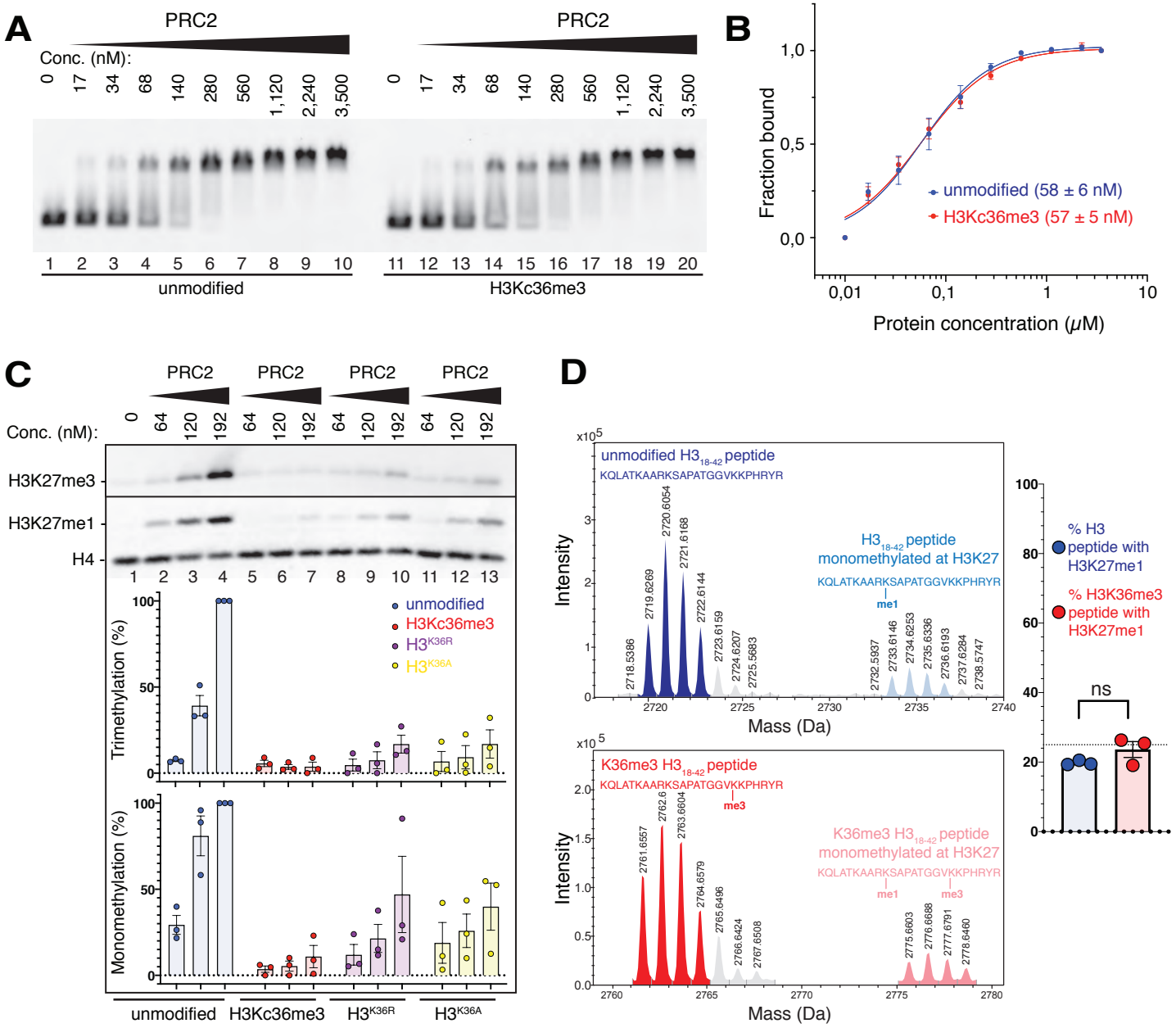
A
PRC2
Conc. (nM):
0 17 34 68 140 280 560 1,120 2,240 3,500
1 2 3 4 5 6 7 8 9 10
unmodified
11 12 13 14 15 16 17 18 19 20
H3Kc36me3
B
Fraction bound
1,0
0,5
0,0
unmodified (58 ± 6 nM)
H3Kc36me3 (57 ± 5 nM)
0,01
0,1
1
10
Protein concentration (μM)
C
PRC2
Conc. (nM):
0 64 120 192
H3K27me3
H3K27me1
H4
1 2 3 4 5 6 7 8 9 10 11 12 13
Trimethylation (%)
Monomethylation (%)
unmodified
H3Kc36me3
H3K36R
H3K36A
D
x10^5
unmodified H3 18-42 peptide
KQLATKAARKSAPATGGVKKPHRYR
H3 18-42 peptide monomethylated at H3K27
me1
Intensity
Mass (Da)
K36me3 H3 18-42 peptide
me3
K36me3 H3 18-42 peptide monomethylated at H3K27
% H3 peptide with H3K27me1
% H3K36me3 peptide with H3K27me1
ns

1077 **FIGURE 3**

1078 **The unmodified H3K36 side chain in the $EZH2_{CXC}$-DNA interaction interface is critical**
1079 **for H3K27 methylation on nucleosomes.**

1080 (**A**, **B**) EMSA analysis and quantification as in **Figure 2A and B**, using PRC2 and
1081 mononucleosomes that were unmodified (lanes 1-10) or contained a trimethyllysine analog at
1082 H3K36 (H3Kc36me3, lanes 11-20).

1083 (**C**) Western Blot (WB) analysis of HMTase reactions with PRC2 as in **Figure 2C** on
1084 unmodified (lanes 1-4), H3Kc36me3 (lanes 5-7), $H3^{K36R}$ (lanes 8-10) or $H3^{K36A}$ (lanes 11-13)
1085 mononucleosomes (446 nM). Coomassie stained gel of reactions is shown in **Supplementary**
1086 **Figure 6A**. Bottom: quantification of H3K27me3 and H3K27me1 chemiluminescence signals,
1087 respectively, by densiometry analysis from three independent experiments. In each experiment,
1088 the methylation signal in lane 4 was defined as 100% and used to quantify the corresponding
1089 H3K27 methylation signals in the other lanes on the same membrane. Circles show individual
1090 data points and error bars SEM.

1091 (**D**) HMTase reactions monitoring H3K27me1 formation by PRC2 on $H3_{18-42}$ peptides that were
1092 unmodified (top) or contained K36me3 (bottom). Left: Deconvoluted ESI-MS spectra from
1093 data shown in **Supplementary Figure 6B**. On both substrates, areas of the four colored peaks
1094 of H3K27me1-modified and unmodified substrate peptides were used for quantification of
1095 H3K27me1 formation. Right: Symbols represent percentages of peptides carrying H3K27me1
1096 in three independent experiments, error bars show SEM; Welch's t-test showed no significant
1097 (ns) difference between H3K27 monomethylation on the two peptide substrates.

1098

1099

1100

Figure 4

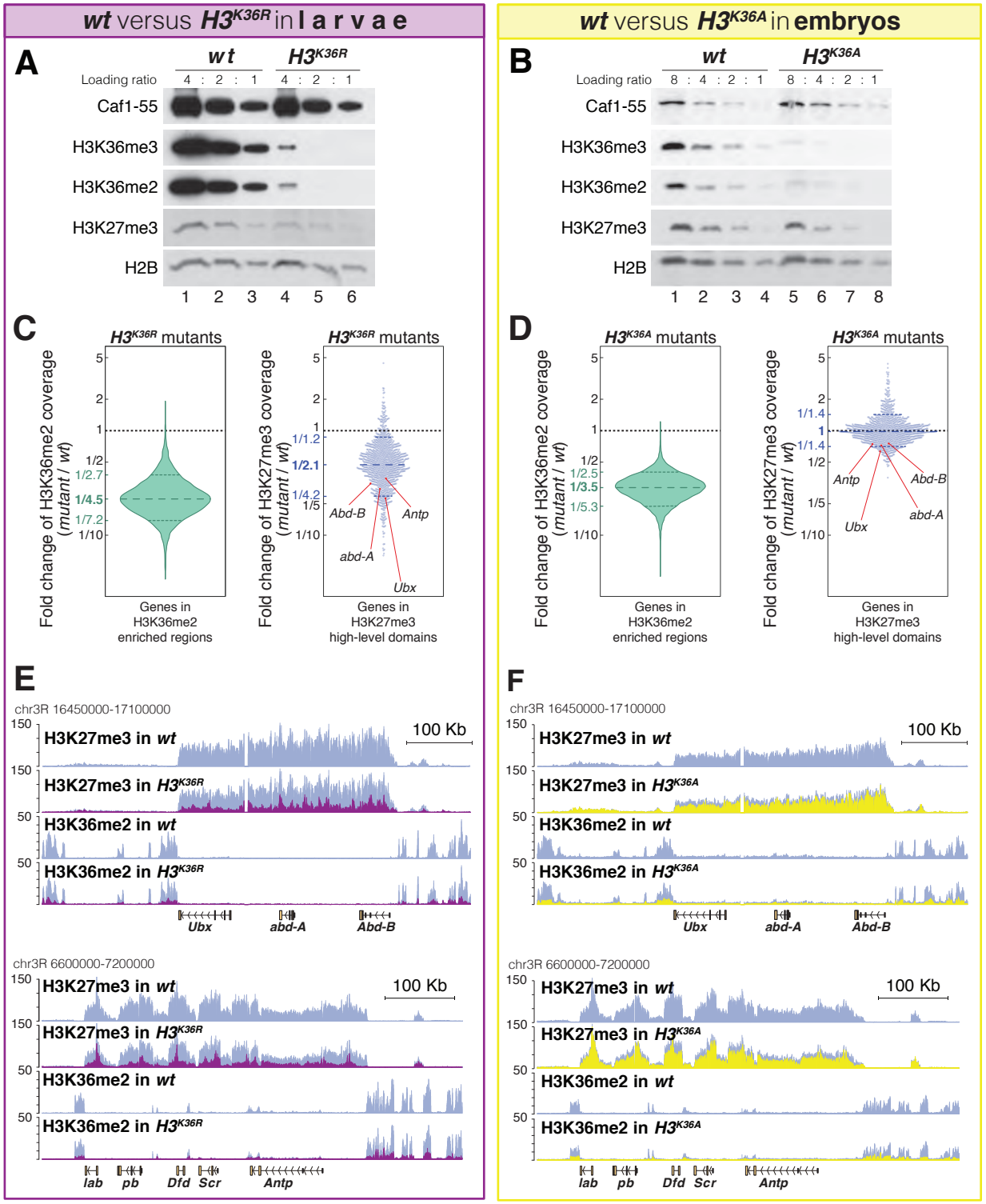
wt versus H3K36R in larvae
wt versus H3K36A in embryos
A
wt
H3K36R
Loading ratio
4 : 2 : 1
4 : 2 : 1
Caf1-55
H3K36me3
H3K36me2
H3K27me3
H2B
1 2 3 4 5 6
B
wt
H3K36A
Loading ratio
8 : 4 : 2 : 1
8 : 4 : 2 : 1
1 2 3 4 5 6 7 8
C
H3K36R mutants
Fold change of H3K36me2 coverage (mutant / wt)
Genes in H3K36me2 enriched regions
Fold change of H3K27me3 coverage (mutant / wt)
Genes in H3K27me3 high-level domains
Abd-B
Antp
abd-A
Ubx
D
H3K36A mutants
Genes in H3K36me2 enriched regions
Genes in H3K27me3 high-level domains
E
chr3R 16450000-17100000
H3K27me3 in wt
H3K27me3 in H3K36R
H3K36me2 in wt
H3K36me2 in H3K36R
100 Kb
Ubx
abd-A
Abd-B
chr3R 6600000-7200000
lab
pb
Dfd
Scr
Antp
F
H3K27me3 in H3K36A
H3K36me2 in H3K36A

1101 **FIGURE 4**

1102 ***H3^{K36A}* and *H3^{K36R}* mutants show reduced levels of H3K27me3.**

1103 (**A**) Western blot analysis on serial dilutions (4:2:1) of total cell extracts from wing, haltere
1104 and 3rd leg imaginal disc tissues dissected from *wildtype* (*wt*, lanes 1-3) and *H3^{K36R}* mutant
1105 (lanes 4-6) third instar larvae. Blots were probed with antibodies against H3K36me3,
1106 H3K36me2 or H3K27me3; in each case, probing of the same membranes with antibodies
1107 against Caf1-55 and H2B served as controls for loading and western blot processing. Note the
1108 reduced levels of H3K36me3 and H3K36me2 but also of H3K27me3 in *H3^{K36R}* mutants
1109 compared to *wildtype* (*wt*) (see text). See Materials and Methods for details of all genotypes.

1110 (**B**) Western blot analysis on serial dilutions (8:4:2:1) of total nuclear extracts from 21-24 hr
1111 old *wt* (lanes 1-4) and *H3^{K36A}* mutant (lanes 5-8) embryos, probed with antibodies against
1112 H3K36me3, H3K36me2 or H3K27me3; and with antibodies against Caf1-55 and H2B as
1113 controls. Note that H3K36me3 and H3K36me2 levels are reduced in *H3^{K36R}* mutants compared
1114 to *wt* but that H3K27me3 levels appear undiminished in the mutant (see text).

1115 (**C**) Left, violin plot showing the fold-change of H3K36me2 coverage in *H3^{K36R}* mutant larvae
1116 relative to *wt* at genes that in wildtype larval CNS and imaginal disc tissues are decorated with
1117 H3K36me2 (see Materials and Methods). The dashed line marks the median reduction (4.5-
1118 fold), the dotted lines indicate indicated the interval comprising 80% of regions. Right, Bee
1119 plot showing the fold-change of H3K27me3 coverage in *H3^{K36R}* mutant larvae relative to *wt* at
1120 genes that in wildype larval CNS and imaginal disc tissues are associated with high-level
1121 H3K27me3 regions (see Materials and Methods). The dashed line marks the median reduction
1122 (2.1-fold), the dotted lines indicate the interval comprising 80% of regions. Note that
1123 H3K27me3 coverage at the HOX genes *abd-A*, *Abd-B*, *Ubx* and *Antp* is between 3- and 4-fold
1124 reduced.

1125 (**D**) Analysis and representation as in (**C**) but showing fold-changes in H3K36me2 and
1126 H3K27me3 coverage in *H3^{K36A}* mutant late-stage embryos relative to *wt* at genes that in
1127 wildtype embryos are decorated with H3K36me2 and H3K27me3, respectively. Note that
1128 H3K27me3 coverage at the HOX genes *abd-A*, *Abd-B*, *Ubx* and *Antp* is about 1.5-fold reduced.

1129 See also **Supplementary Figure 8**.

1130 (**E**) H3K27me3 and H3K36me2 ChIP-seq profiles in larval CNS and imaginal disc tissues
1131 from *wt* (blue) and $H3^{K36R}$ mutant (purple) third instar larvae; in the tracks showing the profiles
1132 in the $H3^{K36R}$ mutant, the *wt* profile is superimposed as reference (see **Table S2** and Materials
1133 and Methods for information about normalization). Top: genomic interval containing the
1134 *Bithorax-Complex* harbouring the HOX genes *Ubx*, *abd-A* and *Abd-B*; bottom: genomic interval
1135 containing the *Antennapedia-Complex* with the HOX genes *lab*, *pb*, *Dfd*, *Scr* and *Antp*. Note
1136 the 3- to 4-fold reduction of H3K27me3 levels across the *Bithorax* and *Antennapedia* loci in
1137 $H3^{K36R}$ mutants. Also note that the analyzed tissues (CNS, thoracic imaginal discs and eye-
1138 antenna discs) represent a mixed population of cells with respect to transcriptionally active and
1139 repressed states of each HOX gene. For each HOX gene there is a substantially larger
1140 proportion of cells in which the gene is decorated with H3K27me3 and repressed by Polycomb
1141 and only a small proportion of cells in which the gene is active and decorated with H3K36me2.

1142 (**F**) H3K27me3 and H3K36me2 ChIP-seq profiles at the *Bithorax* and *Antennapedia* loci as in
1143 (**E**) but from *wt* (blue) and $H3^{K36A}$ mutant (yellow) late-stage embryos with the *wt* profile
1144 superimposed in the tracks showing the profiles in the $H3^{K36A}$ mutant. H3K27me3 levels across
1145 the *Bithorax* and *Antennapedia* loci in $H3^{K36A}$ mutants are only about 1.5-fold reduced
1146 compared to *wt*.

1147

1148

Figure 5

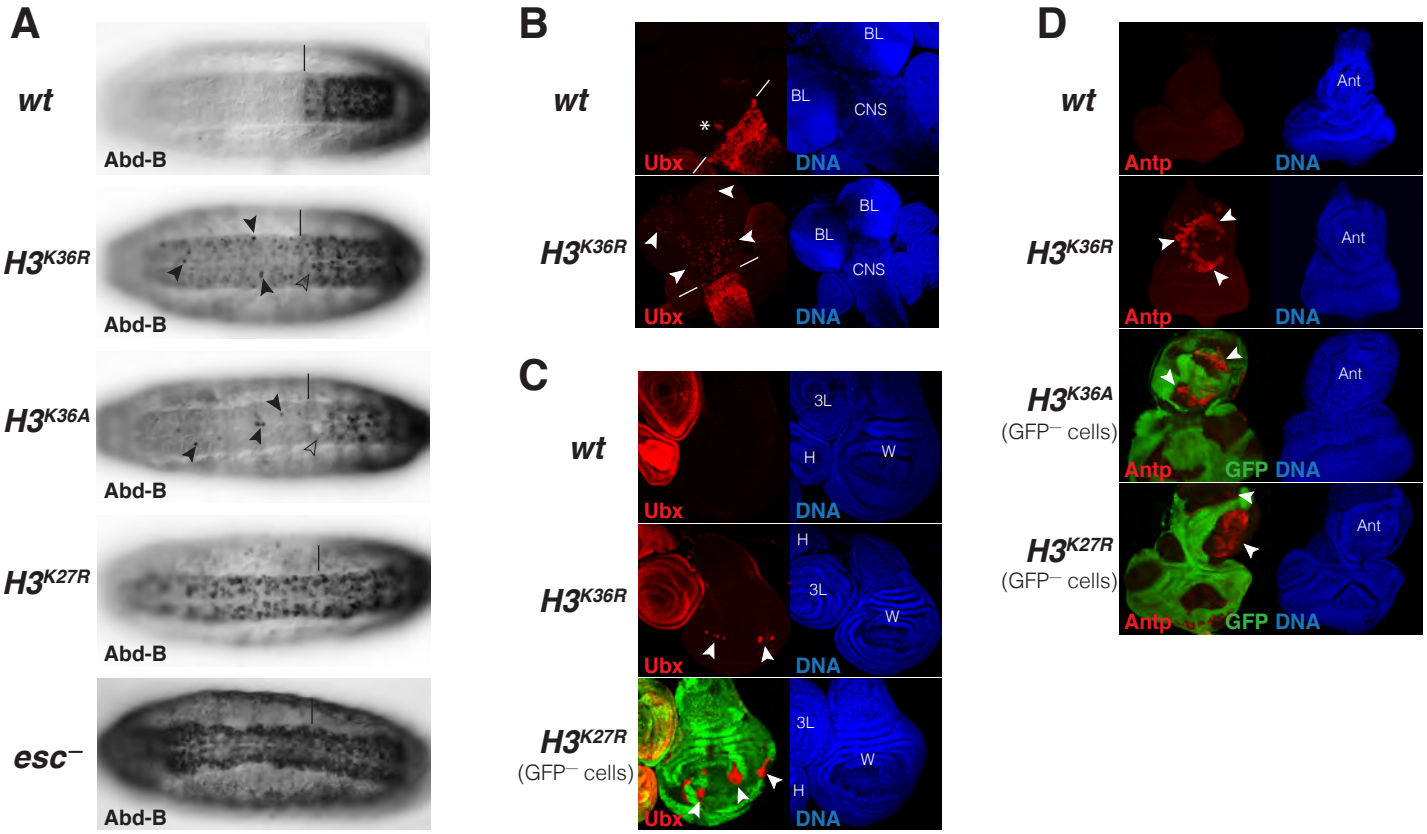
A
wt
Abd-B
H3K36R
Abd-B
H3K36A
Abd-B
H3K27R
Abd-B
esc−
Abd-B
B
wt
Ubx
BL
BL
CNS
DNA
H3K36R
Ubx
BL
BL
CNS
DNA
C
wt
Ubx
3L
H
W
DNA
H3K36R
Ubx
H
3L
W
DNA
H3K27R
(GFP− cells)
Ubx
3L
W
H
DNA
D
wt
Antp
Ant
DNA
H3K36R
Antp
Ant
DNA
H3K36A
(GFP− cells)
Antp
GFP
Ant
DNA
H3K27R
(GFP− cells)
Antp
GFP
Ant
DNA

1149 **FIGURE 5**

1150 ***Drosophila* with H3^{K36R} or H3^{K36A} chromatin show defective Polycomb repression at HOX**

1151 **genes**

1152 (**A**) Ventral views of stage 16 wildtype (*wt*), *H3^{K36A}*, *H3^{K36R}*, *H3^{K27R}* or *esc* (*esc*$^{-}$) mutant

1153 embryos, stained with antibody against Abd-B protein; the *esc* mutant embryo lacked both

1154 maternal and zygotic expression of *esc* (see Materials and Methods for details of all genotypes).

1155 The vertical bar marks the anterior boundary of *Abd-B* expression in parasegment (ps) 10 in *wt*

1156 embryos. Note the stochastic misexpression of Abd-B protein in single cells anterior to ps10

1157 in *H3^{K36R}* and *H3^{K36A}* mutant embryos (arrowheads). *H3^{K27R}* and *esc* mutant embryos show

1158 widespread misexpression of Abd-B protein in the head-to-tail pattern characteristic of PcG

1159 mutants. For reasons that are not well understood, *H3^{K36A}* and *H3^{K36R}* mutants also show partial

1160 loss of Abd-B expression in cells in ps10 (empty arrowheads).

1161 (**B**) Larval CNS and brain lobe tissues from wildtype (*wt*) or *H3^{K36R}* mutant third instar larvae,

1162 stained with antibody against Ubx protein (red) and Hoechst (DNA) to label all nuclei; location

1163 of CNS and brain lobes (BL) are indicated in the right panel. The white bars mark the anterior

1164 boundary of *Ubx* expression in ps5 in *wt* embryos, the asterisk marks the Ubx-expressing cells

1165 in the central midline of ps4 that are part of the wild-type Ubx pattern. Note the stochastic

1166 misexpression of Ubx protein in many single cells anterior to ps5 in the CNS and in the brain

1167 lobes (arrowheads).

1168 (**C**) Imaginal wing (W), haltere (H) and 3rd leg (3L) discs from wildtype (*wt*) or *H3^{K36R}* mutant

1169 third instar larvae and, as reference, discs from a larvae with clones of *H3^{K27R}* mutant cells that

1170 are marked by the absence of GFP. In all cases discs were stained with antibody against Ubx

1171 protein (red) and Hoechst (DNA) to label all nuclei. In *wt* animals, Ubx is expressed in the

1172 halter and 3rd leg disc but not in the wing disc where it is repressed by the PcG machinery. Note

1173 that in *H3^{K36R}* mutants, Ubx is misexpressed in small clusters of cells in the pouch area of the

1174 wing disc (arrowheads) but remains repressed in the rest of the wing disc. Such misexpression

1175 was detected in 50% of wing discs (n = 28). As reference, a wing discs with *H3^{K27R}* mutant

1176 clones is shown, where all cells in the clones in the wing pouch (arrowheads) show

1177 misexpression of Ubx and only mutant cells in the notum and hinge show no misexpression
1178 (empty arrowheads) (cf. (Pengelly et al., 2013)). Also note that in $H3^{K36R}$ mutants (n > 30
1179 mutant animals analysed), Ubx expression in haltere and leg discs appears unperturbed
1180 (asterisks).
1181 (**D**) Eye-antennal imaginal discs from wildtype (*wt*) or $H3^{K36R}$ mutant larvae and below discs
1182 from larvae with clones of $H3^{K36A}$ or $H3^{K27R}$ mutant cells that are marked by the absence of
1183 GFP. All animals were stained with antibody against Antp protein (red) and Hoechst (DNA)
1184 to label all nuclei. Antp is not expressed in the eye-antennal disc of *wt* animals. Note that in
1185 $H3^{K36R}$ mutant discs, Antp is misexpressed in large clusters of cells (arrowheads) in the antenna
1186 primordium (Ant). Note that Antp is also misexpressed in $H3^{K36A}$ or $H3^{K27R}$ mutant cell clones
1187 in the antenna primordium (arrowheads) and that in these cases misexpression also only occurs
1188 in a subset of the mutant cells and not in all clones.
1189
1190
1191
1192
1193

Supplementary Figure 1

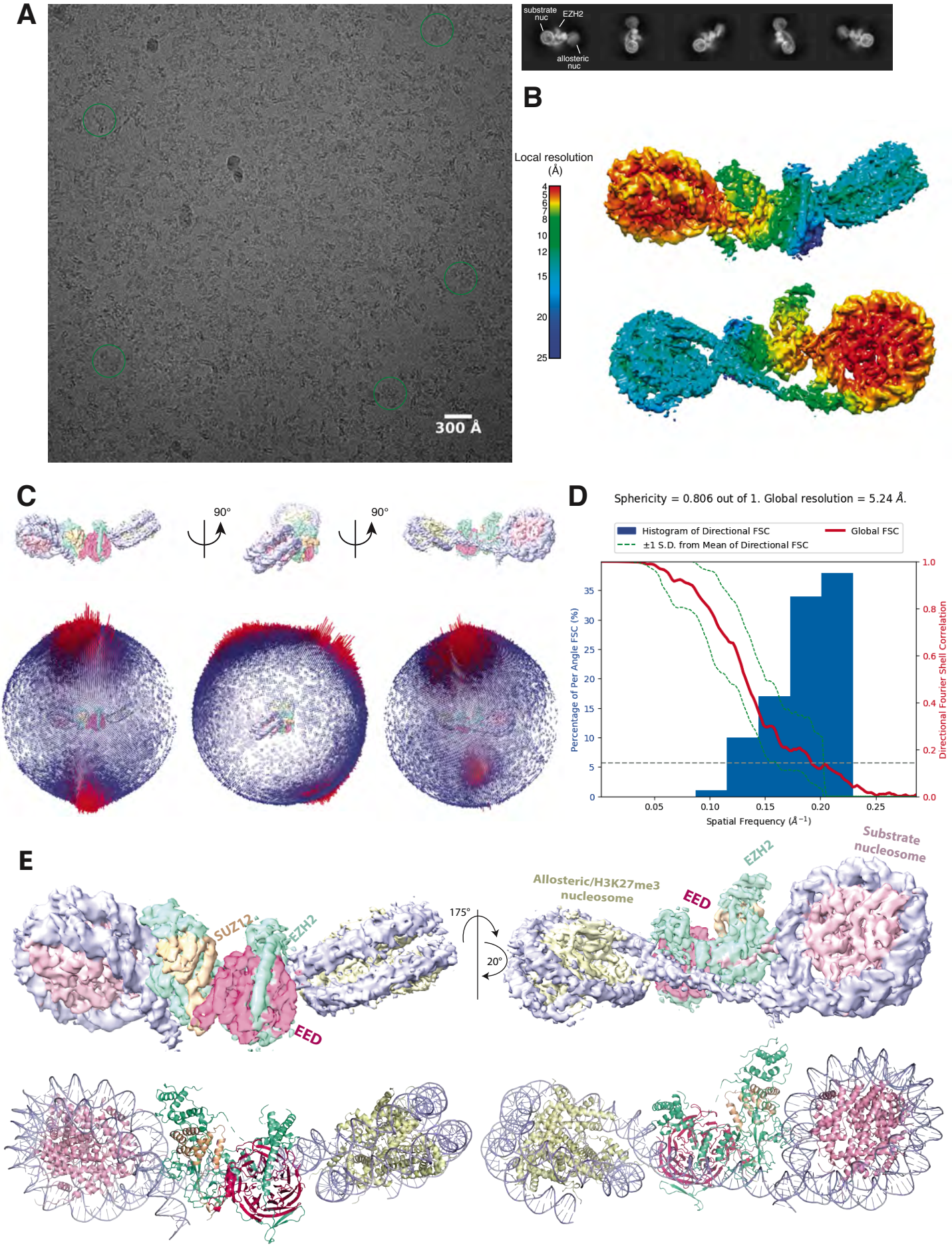

1194 **SUPPLEMENTARY FIGURE 1**
1195
1196 **Initial Cryo-EM analysis of the PHF1-PRC2:di-Nuc complex (related to Fig. 1).**
1197 (**A**) Representative micrograph of the cryo-EM dataset (left) and reference-free 2D classes
1198 from particles picked without templates (right) (performed to ensure that no bias was introduced
1199 through templates picking and references in 3D classification).. Circles indicate particles, which
1200 were picked with templates and directly subjected to 3D analysis (see **fig. S2**).
1201 (**B**) Local resolution estimation of the 5.2 Å overall PHF1-PRC2:di-Nuc map. The substrate
1202 nucleosome and the adjacent part of EZH2 are well resolved (colors red to yellow).
1203 (**C**) Spherical angular distribution of particles included in the final reconstruction of PHF1-
1204 PRC2:di-Nuc.
1205 (**D**) Output from the 3DFSC Processing Server (https://3dfsc.salk.edu/ (Tan et al., 2017))
1206 showing the Fourier Shell Correlation (FSC) as a function of spatial frequency, generated from
1207 masked independent half maps of PRC2:diNuc: global FSC (red), directional FSC (blue
1208 histogram) and deviation from mean (spread, green dotted line). The nominal overall resolution
1209 of 5.24 Å was estimated according to the gold standard FSC cutoff of 0.143 (grey dotted line)
1210 (Rosenthal and Henderson, 2003). Sphericity is an indication for anisotropy and amounts to
1211 0.806 in this data. The minor directional anisotropy of the data can be explained by the slightly
1212 preferred orientation and missing views as seen in (**C**).
1213 (**E**) Top: Refined and postprocessed cryo-EM density map of overall PHF1-PRC2:di-Nuc
1214 colored according to the subunit organization. Bottom: pseudoatomic model of fitted crystal
1215 structure of the human PRC2 catalytic lobe (PDB: 5HYN) and a di-Nuc model with 35 bp linker
1216 DNA (Poepsel et al., 2018), including PDB 1AOI.
1217

Supplementary Figure 2

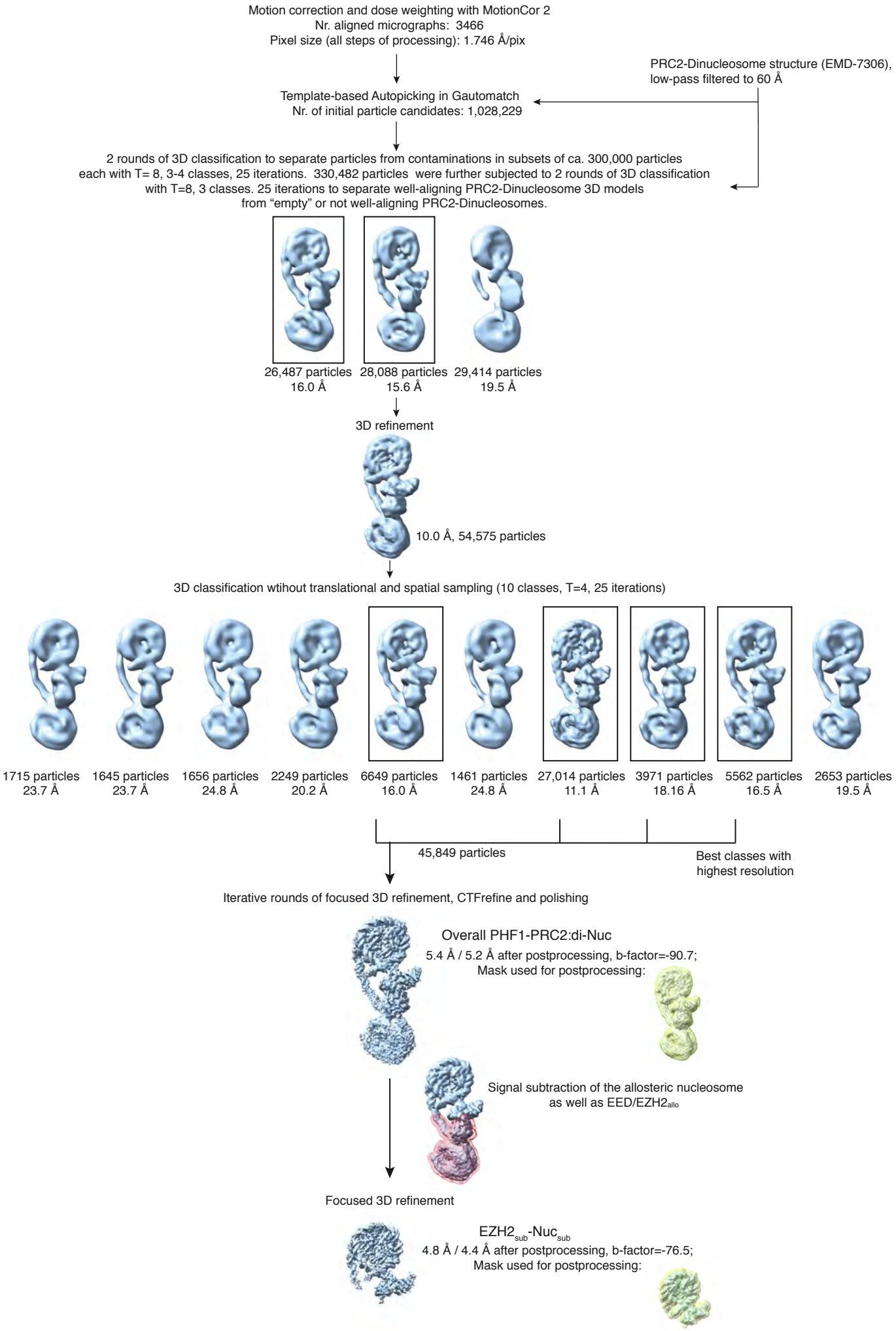

1218 **SUPPLEMENTARY FIGURE 2**
1219
1220 **Overview of the cryo-EM Data-Processing and Particle Sorting Scheme (related to Figure**
1221 **1).**
1222 Processing and particle sorting scheme, also described in Methods. Squares indicate 3D classes
1223 (and corresponding particles) chosen for further processing steps based on their nominal global
1224 resolution values, translational and rotational accuracy and the presence of detailed structural
1225 information. Two final reconstructions were obtained in this study: Overall PHF1-PRC2:di-
1226 Nuc, and $EZH2_{sub}$-Nuc_{sub} after performing signal subtraction (mask indicated in pink) and
1227 focused refinement. Masks used for postprocessing are shown in yellow.
1228

Supplementary Figure 3

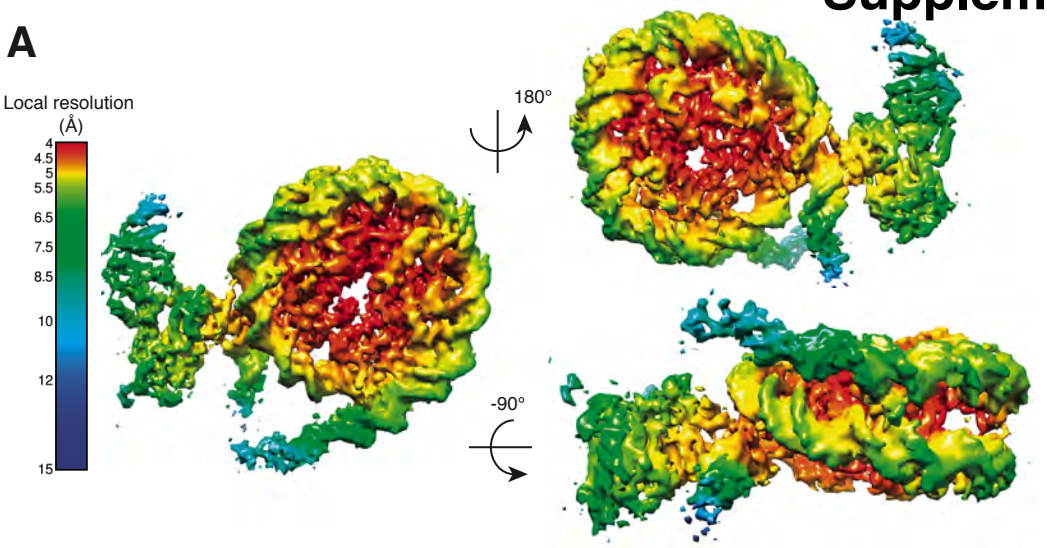

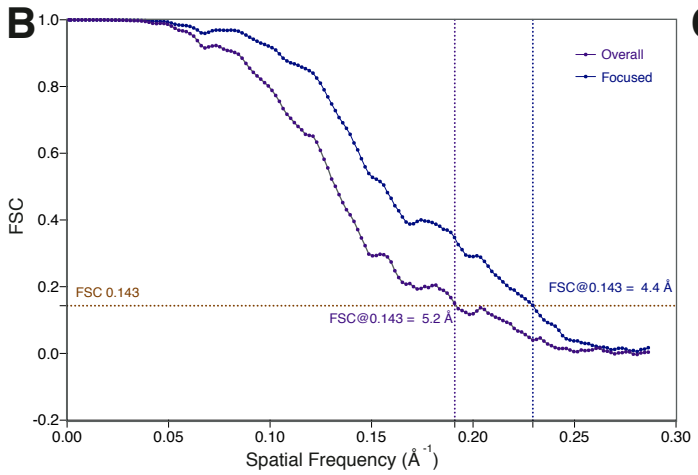

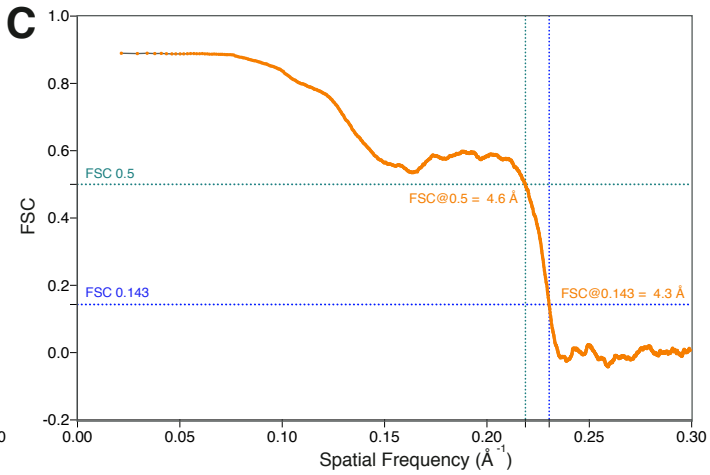

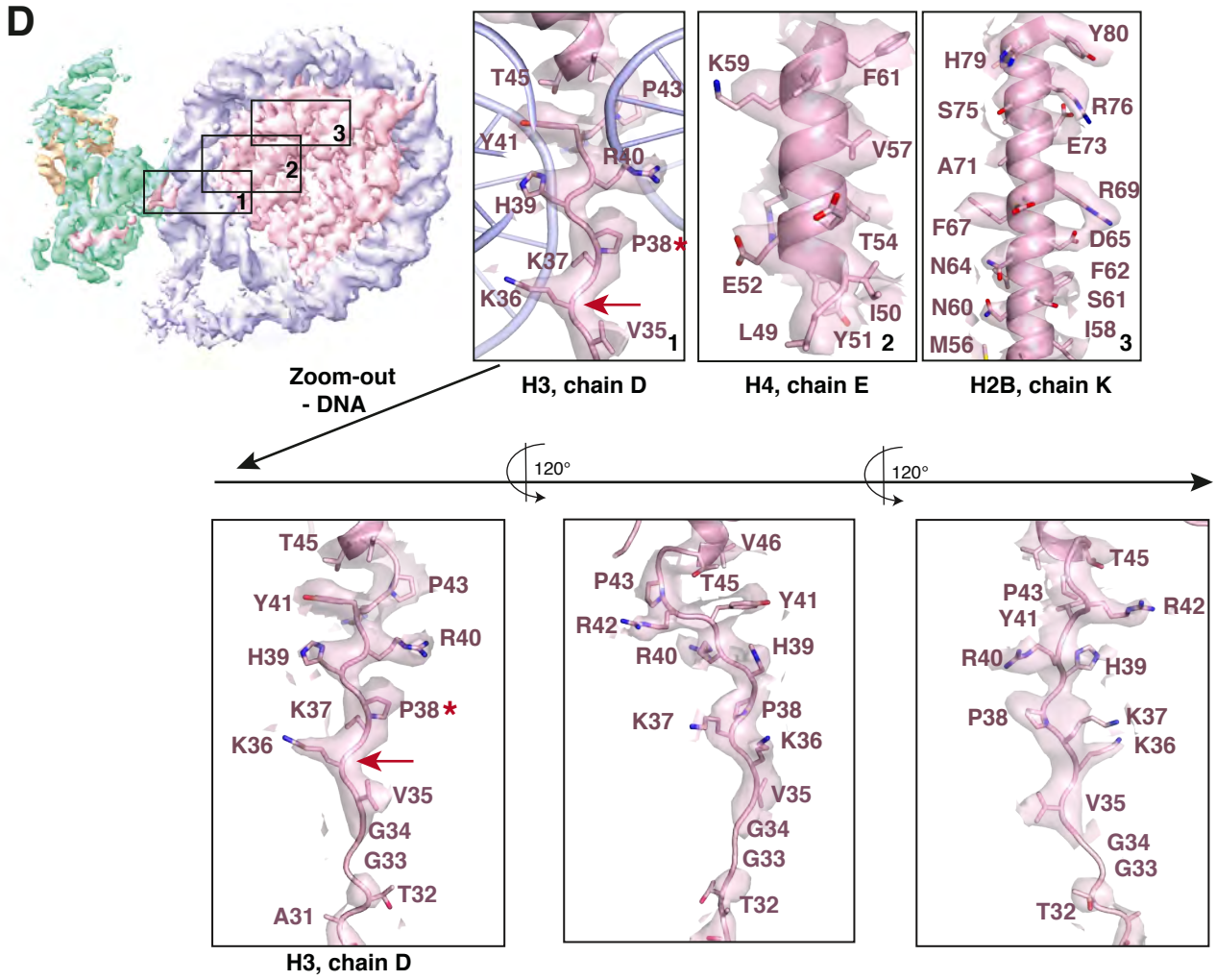

1229 **SUPPLEMENTARY FIGURE 3**
1230
1231 **Cryo-EM analysis of the focused $EZH2_{sub}$-Nuc_{sub} map (related to Fig. 1).**
1232 (**A**) Local resolution estimation of the focused 4.4 Å $EZH2_{sub}$:Nuc_{sub} reconstruction. Regions
1233 in the nucleosome core as well as the adjacent regions including parts of the H3 N-terminus
1234 close to the exit side of the nucleosome are well resolved (4.0 – 5.5 Å). Regions close to the
1235 mask, especially the nucleosomal DNA and parts of EZH2, are less well resolved (colors green
1236 to blue).
1237 (**B**) Global FSC generated from masked independent half maps of $EZH2_{sub}$-Nuc_{sub} (Focused,
1238 blue line) and the overall PHF1-PRC2:di-Nuc (Overall, violet line) were plotted against spatial
1239 frequency. The resolution of 4.4 Å for for $EZH2_{sub}$-Nuc_{sub} map and 5.2 Å for the overall PHF1-
1240 PRC2:di-Nuc map were estimated according to the gold standard FSC cutoff of 0.143 (brown
1241 dotted line) (Rosenthal and Henderson, 2003)
1242 (**C**) FSC between the atomic model and the masked (applied in Phenix) map of $EZH2_{sub}$-Nuc_{sub}
1243 after real-space refinement (Afonine et al., 2018). Green line represents the cut-off at 0.5 (4.6
1244 Å) and blue line represents the cut-off at 0.143 (4.3 Å) (see also Table 1) (Henderson et al.,
1245 2012; Rosenthal and Henderson, 2003; Rosenthal and Rubinstein, 2015).
1246 **(D)** Selected regions within $EZH2_{sub}$-Nuc_{sub} showing side chain density, e.g. K36 (red arrow).
1247 A red asterisk indicates the last residue of the H3 tail visible in known crystal structures (usually
1248 P38 or H39). The quality of the map around K36 is shown as a separate zoom-out below and
1249 in three different views to demonstrate the lack of anisotropy present in the density.
1250
1251
1252

Supplementary Figure 4

A. Front view/CXC

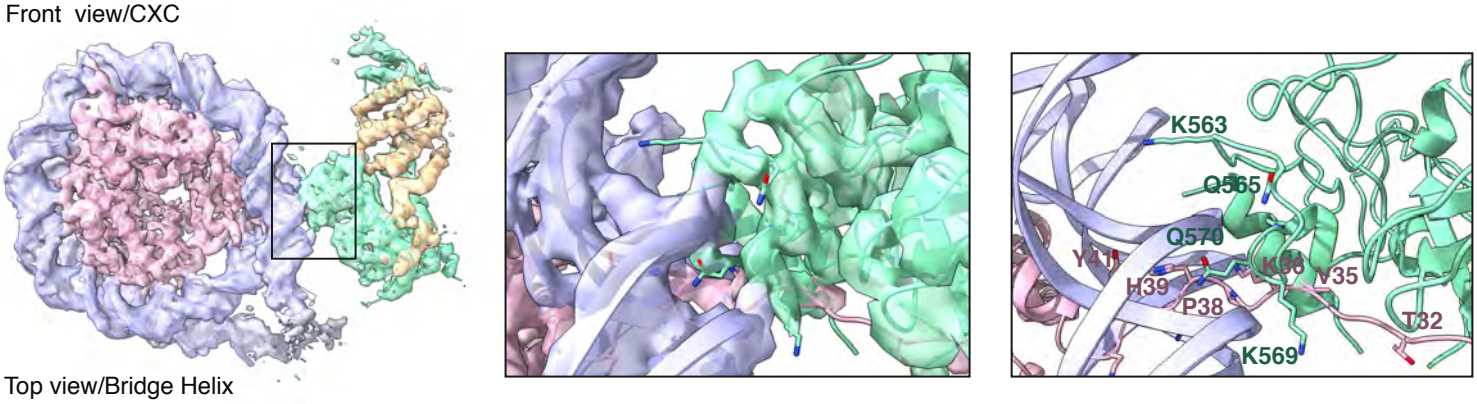

B. Top view/Bridge Helix

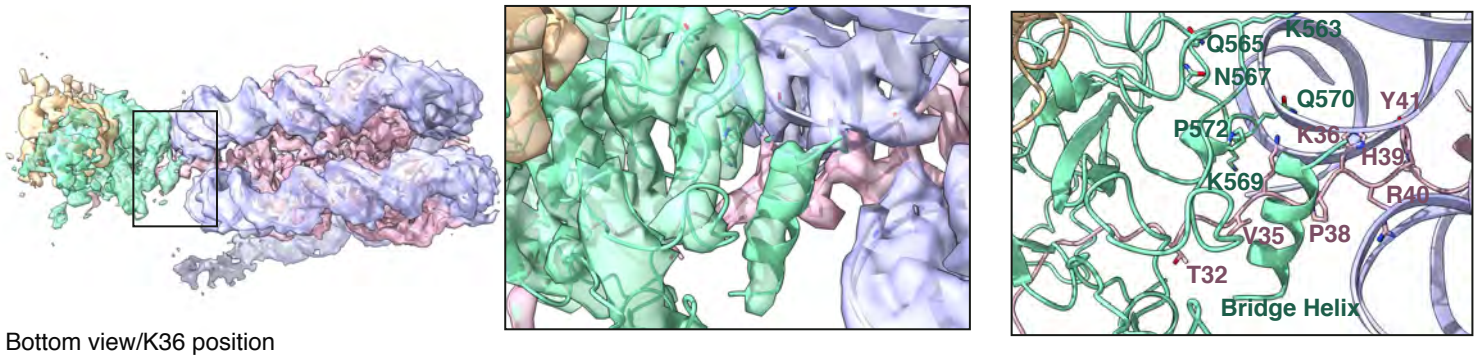

C. Bottom view/K36 position

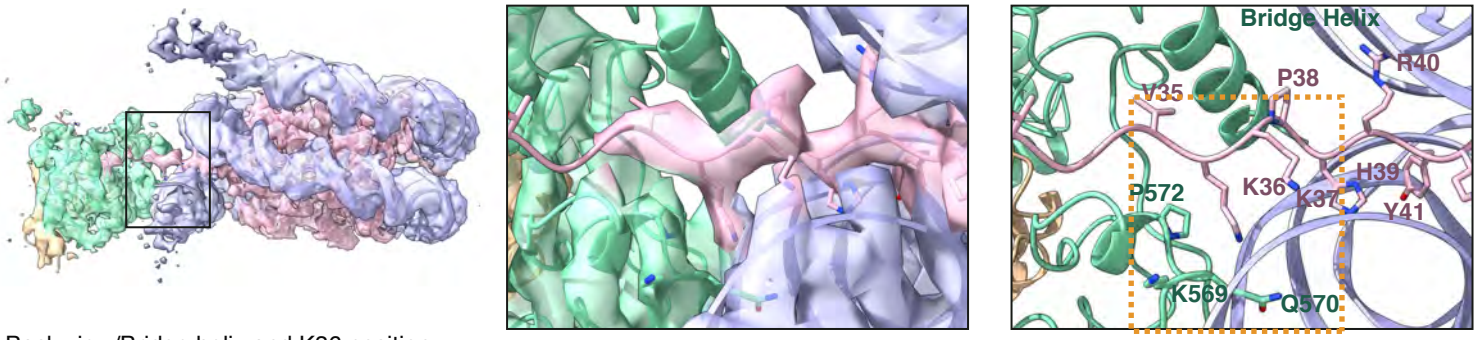

D. Back view/Bridge helix and K36 position

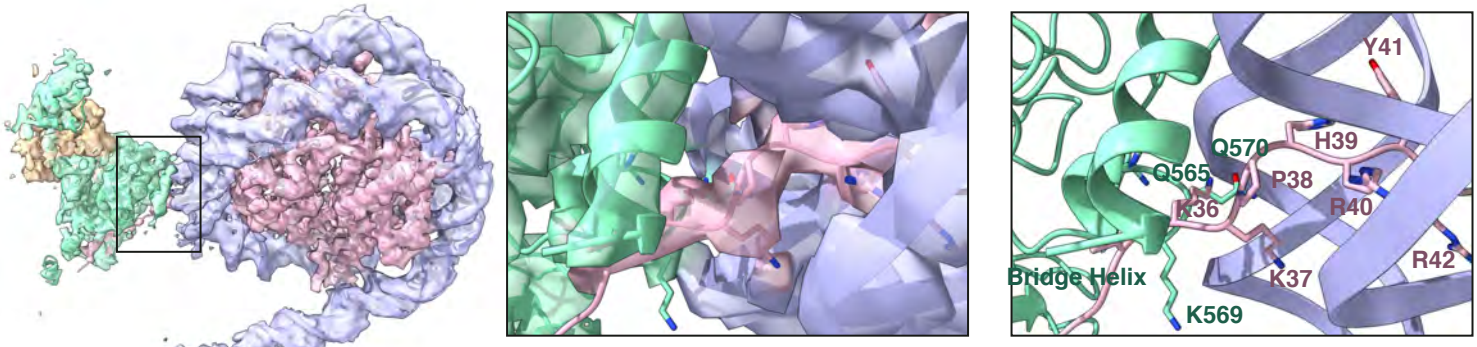

E.

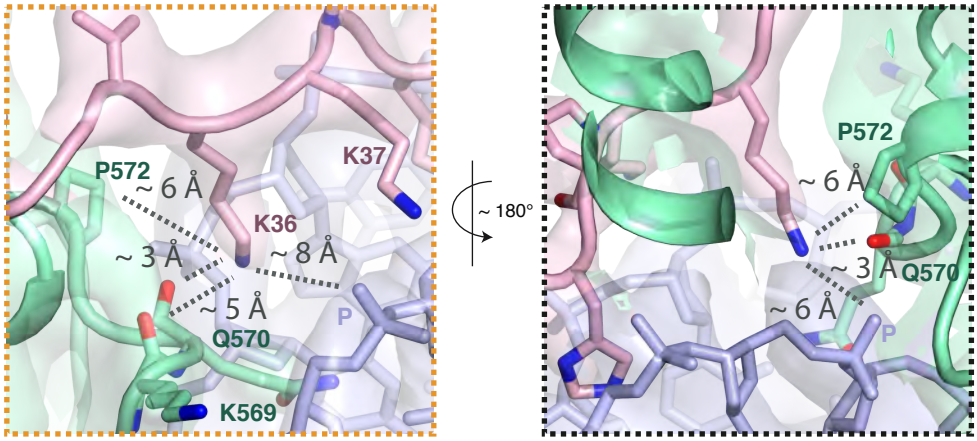

F.

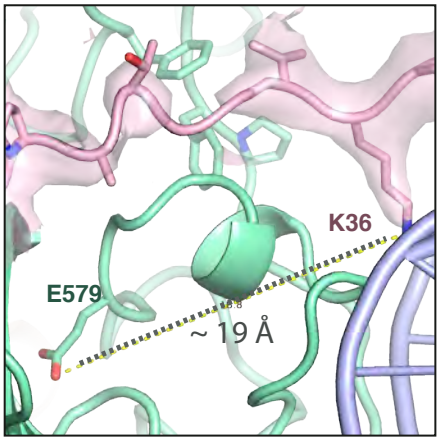

H3 tail/E579 pocket

1253 **SUPPLEMENTARY FIGURE 4**
1254
1255 **The improved map of the interaction between EZH2 and the substrate nucleosome**
1256 **after focused refinement reveals location of H3K36 and it's environment (related to Fig.**
1257 **1).**
1258 (**A**) The front view of $EZH2_{sub}$-Nuc_{sub} cryo-EM density and model shows details of the
1259 $EZH2_{CXC}$ interaction with nucleosomal DNA.
1260 (**B**) The top view of $EZH2_{sub}$-Nuc_{sub} cryo-EM shows a tubular density into which based on
1261 recent findings of (Kasinath et al., 2020) a helix was built. The bridge helix, which based on
1262 this study is likely constituted of the EZH2 residues 497-511, is located above V35 of the H3
1263 tail. As can be seen when observing the density-modified map (Terwilliger et al., 2019) of
1264 $EZH2_{sub}$-Nuc_{sub} at lower threshold, it presumably engages in interactions with the nucleosomal
1265 DNA, the H3 tail and EZH2, as described in greater detail in (Kasinath et al., 2020).
1266 (**C**) The bottom view of $EZH2_{sub}$-Nuc_{sub} cryo-EM density and model shows details of the
1267 vicinity of K36 with the corresponding density for the H3 tail, EZH2 and nucleosomal DNA.
1268 The orange square indicates the region shown as a zoom-in in (**E**).
1269 (**D**) The back view of $EZH2_{sub}$-Nuc_{sub} cryo-EM density and model shows details of the location
1270 of K36 and the bridge helix.
1271 (**E**) Zoom-in views of H3K36 and it's chemical environment. Approximate distances of the
1272 epsilon-amino group of H3K36 to the nearest residues are indicated with a dotted grey line.
1273 (**F**) Location of the Glu-579 pocket (Jani et al., 2019) in the $EZH2_{sub}$:Nuc_{sub} reconstruction and
1274 it's distance to H3K36 (app. 19 Å). The described mechanism by Jani et al (Jani et al., 2019)
1275 involving recognition of H3K36 by Glu-579 is incompatible with the presented structural data
1276 as the location differs significantly and major rearrangements as the relocation of the helix-loop
1277 region between residues 564-576 would be necessary to avoid the given steric and geometric
1278 hindrance and allow for potential interaction.
1279

Supplementary Figure 5

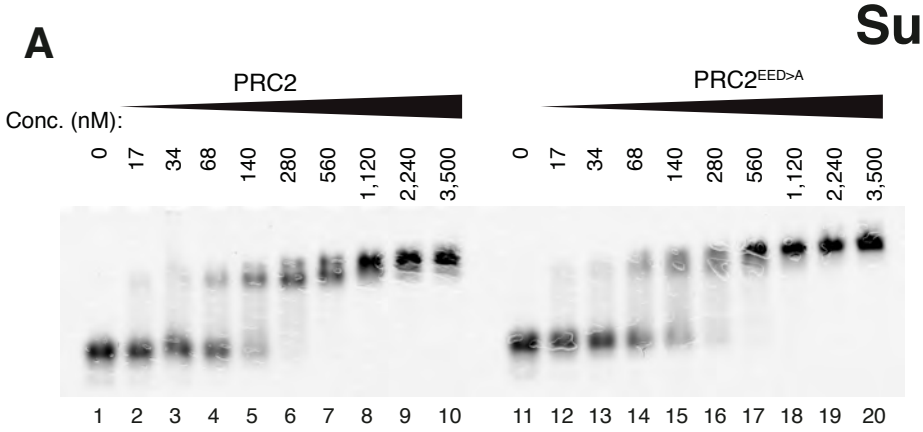

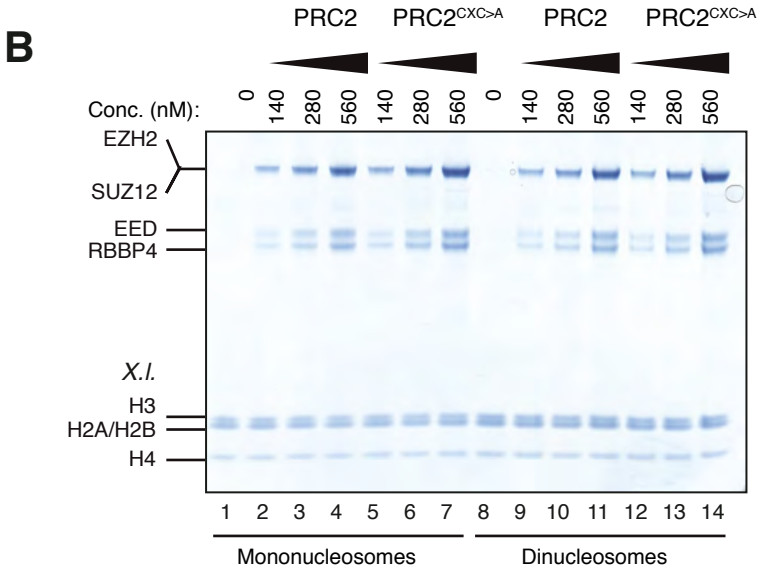

1280 **SUPPLEMENTARY FIGURE 5**
1281
1282 **The $EZH2_{CXC}$-DNA interaction interface is critical for H3K27 methylation on**
1283 **nucleosomes (related to Fig. 2).**
1284 **(A)** Binding reactions with indicated concentrations of PRC2 (lanes 1-10) or $PRC2^{EED>A}$ (lanes
1285 11-20) and 45 nM 6-carboxyfluorescein-labeled mononucleosomes, analyzed by EMSA on
1286 1.2% agarose gels.
1287 (**B**) Coomassie-stained 4-12% SDS-PAGE of the HMTase reactions shown in **Fig. 2C**. *Xenopus*
1288 *laevis* (*X.l.*) nucleosomes were used for these experiments. The short 5-kDa PHF_C fragment is
1289 not visible on this gel.
1290
1291
1292

Supplementary Figure 6

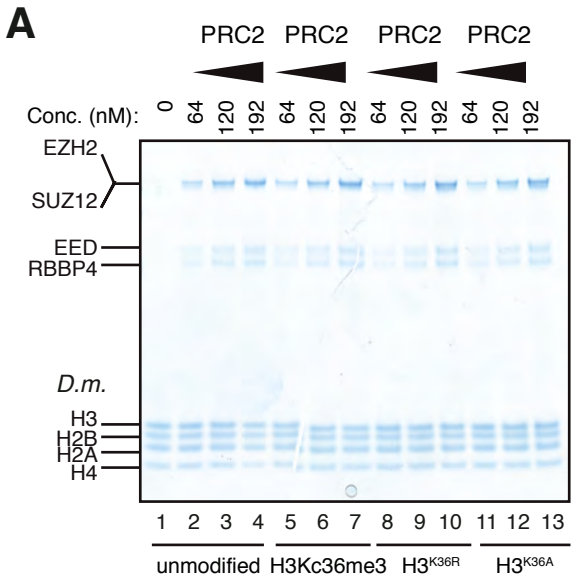

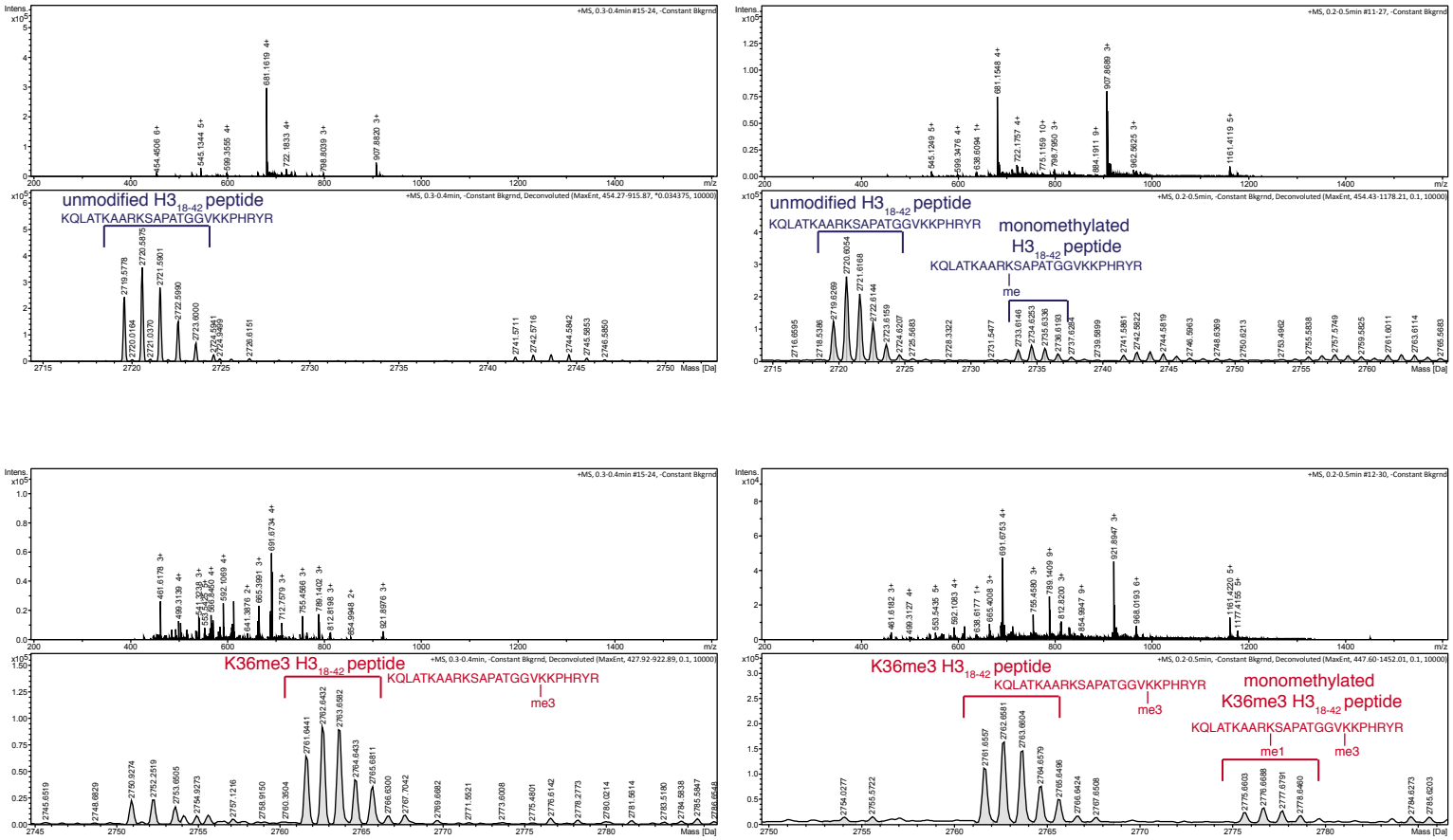

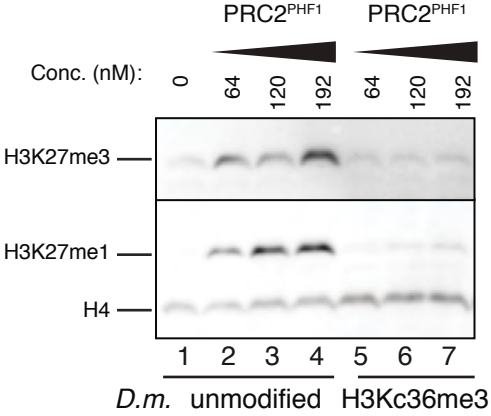

1293 **SUPPLEMENTARY FIGURE 6**
1294
1295 **Accommodation of unmodified H3K36 in the $EZH2_{CXC}$-DNA interaction interface is**
1296 **essential for H3K27 methylation on nucleosomes and PHF1-PRC2 (related to Fig. 3).**
1297 (**A**) Coomassie-stained 4-12% SDS-PAGE of the HMTase reactions shown in **Fig. 3C**.
1298 *Drosophila melanogaster* (*D.m.*) nucleosomes were used for these experiments. The short 5-
1299 kDa PHF_C fragment is not visible on this gel.
1300 (**B**) Full ESI MS spectra (upper part) and full deconvoluted MS spectra (lower part) shown for
1301 input peptides without PRC2 as a control (left) and with PRC2 (right) to ensure no overlapping
1302 between possible adduct peaks and monomethylation peaks.
1303 (**C**) Western Blot (WB) analysis of HMTase reactions with full-length PHF1-PRC2 on
1304 unmodified (lanes 1-4) or H3Kc36me3 (lanes 5-7) mononucleosomes (446 nM).
1305
1306
1307

Supplementary Figure 7

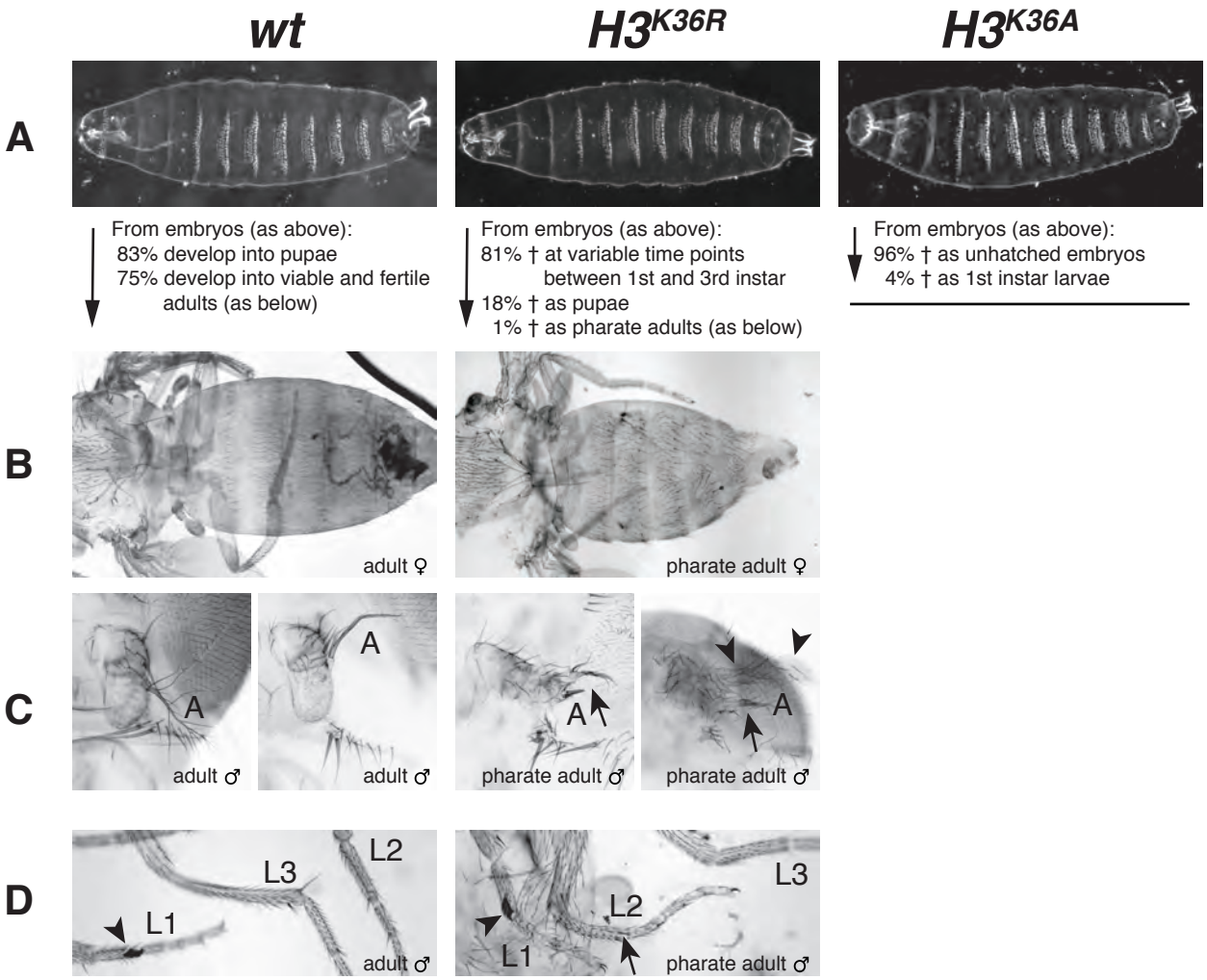

1308 **SUPPLEMENTARY FIGURE 7**
1309
1310 ***Drosophila* with H3^{K36R} or H3^{K36A} mutant chromatin arrest development at different**
1311 **stages**
1312 (**A**) Ventral views of cuticles from wildtype (*wt*), *H3*^{K36R}, or *H3*^{K36A} mutant embryos. Note that
1313 the cuticle pattern of the mutant animals is indistinguishable from that of the *wt* embryo.
1314 Below: for each genotype, the fraction of embryos that developed into larve, pupae, pharate
1315 adults or viable adults is listed. The fraction was determined by monitoring the development
1316 of collected hatched 1st instar larvae (*wt*: *n*=300, *H3*^{K36R}: *n*=2000) or unhatched embryos
1317 (*H3*^{K36A}: *n*=200). The GFP marker on the Balancer chromosomes was used for identifying
1318 *H3*^{K36R} and or *H3*^{K36A} mutants.
1319 (**B**) Dorsal views of the posterior portion of the thorax and of the abdomen. From 2000 hatched
1320 *H3*^{K36R} mutant 1st instar larvae, a total of 18 pharate adults was recovered. Most *H3*^{K36R} mutant
1321 pharate adults showed a relatively normal overall body patterning apart from the homeotic
1322 transformations illustrated below.
1323 (**C**) Frontal view of adult heads illustrating the antenna-to-leg transformation in *H3*^{K36R} mutant
1324 pharate adults. The antenna-to-leg transformation in *H3*^{K36R} mutant animals ranged from mild
1325 (arrows) to more extensive transformations with formation of leg-like structures such as in this
1326 extreme case (arrowheads).
1327 (**D**) The sex comb in males is normally only present on the protoracic (L1) legs (arrowheads).
1328 Among the *H3*^{K36R} mutant pharate adult males recovered (*n*=13), five showed one or several
1329 extra sex comb teeth (arrow) on the meso- (L2) or metathoracic (L3) legs. Extra sex comb teeth
1330 in adults are a hallmark phenotype of Polycomb mutants.
1331
1332

Supplementary Figure 8

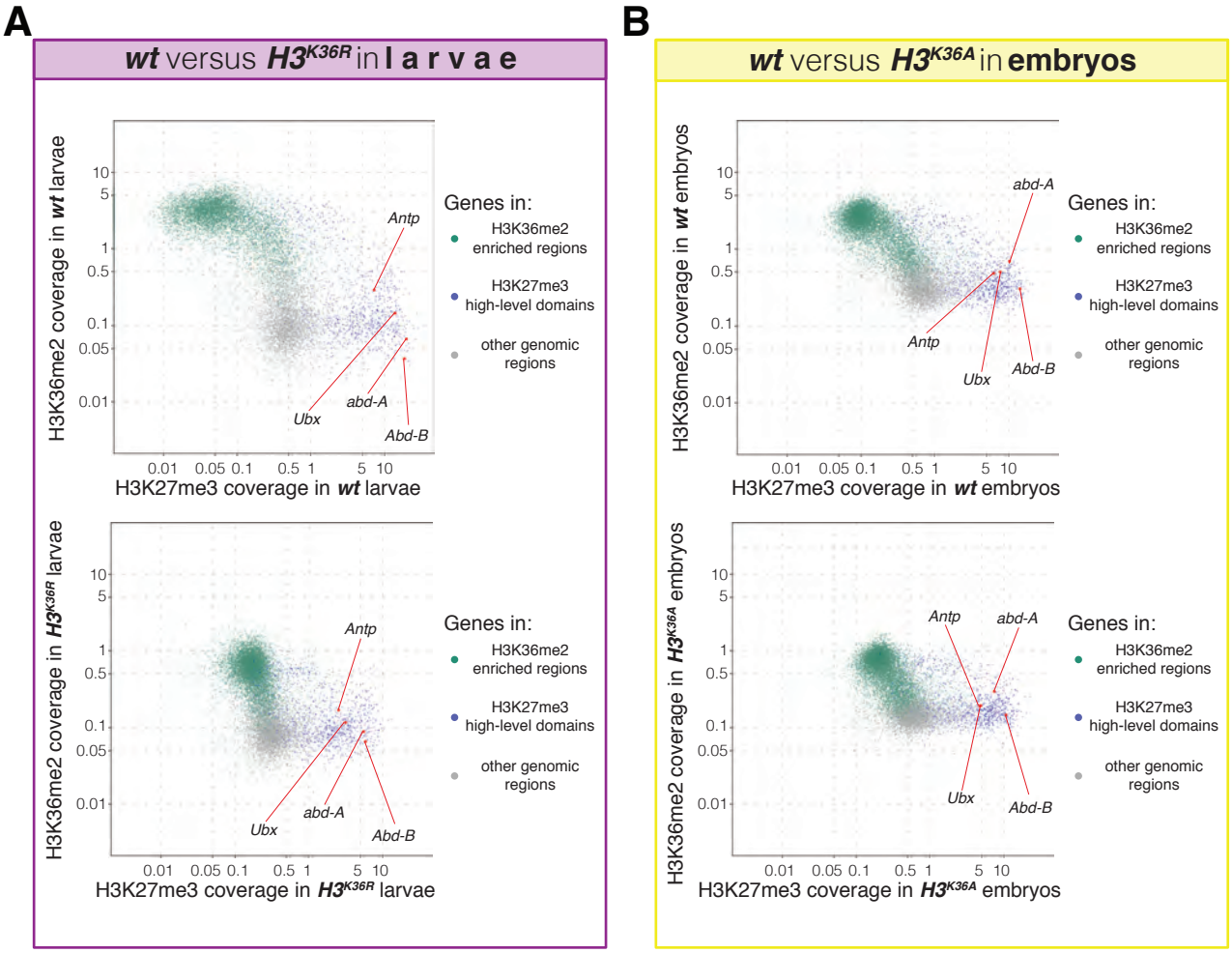

1333 **SUPPLEMENTARY FIGURE 8**
1334
1335 ***H3^{K36R}* and *H3^{K36A}* mutants show altered H3K36me2 and H3K27me3 profiles (related to**
1336 **Fig. 4)**
1337 (**A**) Top, scatter plots showing H3K36me2 coverage in relation to H3K27me3 coverage in *wt*
1338 larvae. Green dots represent 9200 gene bodies overlapping with genomic intervals showing
1339 H3K36me2 enrichment, blue dots represent 1030 gene bodies overlapping with genomic
1340 intervals defined as high-level H3K27me3 domains (Bonnet et al., 2019), and grey dots
1341 represent 6300 gene bodies showing no enrichment for either methylation mark in larvae (see
1342 Materials and Methods). Bottom, scatter plot showing the H3K36me2 read coverage in relation
1343 to H3K27me3 read coverage in *H3^{K36R}* mutant larvae.
1344 (**B**) As in (**A**) but showing H3K36me2 coverage in relation to H3K27me3 coverage in *wt*
1345 embryos (top) and in *H3^{K36A}* mutant embryos (bottom). Green dots represent 10800 gene bodies
1346 overlapping with genomic intervals showing H3K36me2 enrichment, blue dots represent 1030
1347 gene bodies overlapping with genomic intervals defined as high-level H3K27me3 domains
1348 (Bonnet et al., 2019), and grey dots represent 5400 gene bodies showing no enrichment for
1349 either methylation mark in embryos (see Materials and Methods).
1350
1351
1352
1353

1354 **Table S1**

1355

1356 **Cryo electron microscopy data collection summary, processing statistics and model**

Cryo electron microscopy data collection (applicable to Overall PHF1-PRC2:diNuc and $EZH2_{sub}$-Nuc_{sub} maps)		
Microscope	FEI Titan Krios GII	
Voltage (kV)	300	
Camera	Gatan K2-Summit	
Energy Filter	Gatan Quantum-LS (GIF)	
Pixel size (Å/pix) (calibrated)	1.75	
Nominal magnification (x)	81000	
Preset target global defocus range (µm)	0.5 - 3.5	
Total electron exposure (fluence, $e^-/Å^2$)	52,96	
Exposure rate (flux) ($e^-/Å^2/s$)	3,47	
Nr. of frames collected per micrograph	60	
Energy filter slit width (eV)	20	
Automation Software	SerialEM	
3D reconstruction (applicable to Overall PHF1-PRC2:diNuc and $EZH2_{sub}$-Nuc_{sub} maps)		
Number of movies	3466	
Initially selected particle candidates	1,028,229	
Final number of particles	45,849	
	Overall PHF1-PRC2:diNuc	**$EZH2_{sub}$-Nuc_{sub}**
Resolution FSC independent halfmaps (0.143) masked (Å)[a]	5.24	4.36
Local resolution range (Å)	4.01 - 24.97	4.01 – 15.00
Sharpening B-factor ($Å^2$)	-90.7	-76.5
Refinement **$EZH2_{sub}$-Nuc_{sub}**		
No. atoms		28866 (Hydrogens: 13086)
Residues		Protein: 1171 Nucleotide: 312
Ligands		ZN: 8
CC_{mask}, CC_{box}, CC_{peaks}, CC_{volume}[b]		0.75, 0.83, 0.66, 0.74
Mean CC for ligands		0.72
Resolution FSC masked map vs. model (0/0.143/0.5) (Å)[b]		4.3/4.3/4.6
R.m.s. deviations		
Bond lengths (Å)		0.004
Bond angles (°)		0.642
Ramachandran favored (%)		97.51
Ramachandran gen. allowed (%)		2.32
Ramachandran disallowed (%)		0.17

MolProbity score		1.53
Clash score		7.97
ADP (B factors)		
Iso/Aniso (#)		15925/0
Min/max/mean		
Protein		65.89/264.21/121.82
Nucleotide		97.31/221.62/132.65
Ligand		151.54/251.77/201.51
Rotamer outliers (%)		0.00
Cβ outliers (%)		0.00
CaBLAM outliers (%)		1.59

[a]according to the Fourier Shell Correlation (FSC) cut-off criterion of 0.143 defined in (Rosenthal and Henderson, 2003)
[b]according to the map-vs.-model Correlation Coefficient definitions in (Afonine et al., 2018a)

1360 **Table S2.**
1361
1362 **Number of aligned reads to the *D. melanogaster* and *D. pseudoobscura* genomes from**
1363 **ChIP and input datasets and normalization process (related to Figure 4 and**
1364 **Supplementary Figure 8).**
1365
1366

1367 **Movie S1**
1368
1369 **Cryo-EM structure of the PHF1-PRC2:di-Nuc complex (related to Figure 1).**
1370